Testing the Interaction between a Substellar Companion and a Debris Disk in the HR 2562 System

Stella Yimiao Zhang[1], Gaspard Duchêne[2,3], Robert J. De Rosa[4], Megan Ansdell[5], Quinn Konopacky[1],
Thomas Esposito[2,6], Eugene Chiang[7], Malena Rice[8], Brenda Matthews[9], Paul Kalas[2,6,10], Bruce Macintosh[11],
Franck Marchis[6], Stan Metchev[12], Jenny Patience[13], Julien Rameau[3], Kimberly Ward-Duong[14], Schuyler Wolff[15],
Michael P. Fitzgerald[16], Vanessa P. Bailey[17], Travis S. Barman[18], Joanna Bulger[19], Christine H. Chen[20],
Jeffrey K. Chilcotte[21], Tara Cotten[22], René Doyon[23], Katherine B. Follette[24], Benjamin L. Gerard[25,26],
Stephen Goodsell[27,28], James R. Graham[2], Alexandra Z. Greenbaum[29], Pascale Hibon[4], Li-Wei Hung[30],
Patrick Ingraham[31], Jérôme Maire[1], Mark S. Marley[32], Christian Marois[9,25], Maxwell A. Millar-Blanchaer[33],
Eric L. Nielsen[34], Rebecca Oppenheimer[35], David W. Palmer[36], Marshall D. Perrin[37], Lisa A. Poyneer[36], Laurent Pueyo[37],
Abhijith Rajan[37], Fredrik T. Rantakyrö[28], Jean-Baptiste Ruffio[38], Dmitry Savransky[39], Adam C. Schneider[40,41],
Anand Sivaramakrishnan[37], Inseok Song[22], Remi Soummer[37], Sandrine Thomas[31], Jason J. Wang[38,42], and
Sloane J. Wiktorowicz[43]

[1] Center for Astrophysics and Space Sciences, University of California, San Diego, La Jolla, CA 92093, USA; yiz020@ucsd.edu
[2] Astronomy Department, University of California, Berkeley, CA 94720, USA
[3] Univ. Grenoble Alpes/CNRS, IPAG, F-38000 Grenoble, France
[4] European Southern Observatory, Alonso de Córdova 3107, Vitacura, Santiago, Chile
[5] NASA Headquarters, 300 E Street SW, Washington, DC 20546, USA
[6] SETI Institute, Carl Sagan Center, 189 Bernardo Av, Suite 200, Mountain View, CA 94043, USA
[7] Department of Astronomy, UC Berkeley, Berkeley, CA 94720, USA
[8] Department of Astronomy, Yale University, New Haven, CT 06511, USA
[9] Herzberg Astronomy and Astrophysics, National Research Council of Canada, 5071 West Saanich Road, Victoria, BC V9E 2E7, Canada
[10] Institute of Astrophysics, FORTH, GR-71110 Heraklion, Greece
[11] Kavli Institute for Particle Astrophysics and Cosmology, Department of Physics, Stanford University, Stanford, CA 94305, USA
[12] Department of Physics & Astronomy, Institute for Earth and Space Exploration, The University of Western Ontario, London, ON N6A 3K7, Canada
[13] School of Earth and Space Exploration, Arizona State University, PO Box 871404, Tempe, AZ 85287, USA
[14] Smith College, 10 Elm Street, Northampton, MA 01063, USA
[15] Steward Observatory, University of Arizona, Tucson, AZ 85721, USA
[16] Department of Physics & Astronomy, University of California, Los Angeles, CA 90095, USA
[17] Jet Propulsion Laboratory, California Institute of Technology, 4800 Oak Grove Drive, Pasadena, CA 91109, USA
[18] Lunar and Planetary Lab, University of Arizona, Tucson, AZ 85721, USA
[19] Institute for Astronomy, University of Hawai'i, 2680 Woodlawn Drive, Honolulu, HI 96822, USA
[20] Space Telescope Science Institute, 3700 San Martin Drive, Baltimore, MD 21218 USA
[21] Department of Physics and Astronomy, University of Notre Dame, 225 Nieuwland Science Hall, Notre Dame, IN, 46556, USA
[22] Department of Physics and Astronomy, University of Georgia, Athens, GA 30602, USA
[23] Institut de Recherche sur les Exoplanètes, Département de physique, Université de Montréal, Montréal, QC H3C 3J7, Canada
[24] Physics and Astronomy Department, Amherst College, 25 East Drive, Amherst, MA 01002, USA
[25] University of Victoria, Department of Physics and Astronomy, 3800 Finnerty Road, Victoria, BC V8P 5C2, Canada
[26] National Research Council of Canada Herzberg, 5071 West Saanich Road, Victoria, BC V9E 2E7, Canada
[27] Department of Physics, Durham University, Stockton Road, Durham DH1, UK
[28] Gemini Observatory, Casilla 603, La Serena, Chile
[29] IPAC, Mail Code 100-22, Caltech, 1200 E. California Blvd., Pasadena, CA 91125, USA
[30] Natural Sounds and Night Skies Division, National Park Service, Fort Collins, CO 80525, USA
[31] Vera C. Rubin Observatory, 950 N Cherry Ave., Tucson, AZ 85719, USA
[32] Space Science Division, NASA Ames Research Center, Mail Stop 245-3, Moffett Field, CA 94035, USA
[33] Department of Physics, University of California, Santa Barbara, Santa Barbara, CA, USA
[34] Department of Astronomy, New Mexico State University, 1320 Frenger Mall, Las Cruces, NM 88003-8001, USA
[35] American Museum of Natural History, Department of Astrophysics, Central Park West at 79th Street, New York, NY 10024, USA
[36] Lawrence Livermore National Laboratory, 7000 East Ave., Livermore, CA 94550, USA
[37] Space Telescope Science Institute, 3700 San Martin Drive, Baltimore, MD 21218, USA
[38] Department of Astronomy, California Institute of Technology, Pasadena, CA 91125, USA
[39] Sibley School of Mechanical and Aerospace Engineering, Cornell University, Ithaca, NY 14853, USA
[40] US Naval Observatory, Flagstaff Station, P.O. Box 1149, Flagstaff, AZ 86002, USA
[41] Department of Physics and Astronomy, George Mason University, MS3F3, 4400 University Drive, Fairfax, VA 22030, USA
[42] Center for Interdisciplinary Exploration and Research in Astrophysics (CIERA) and Department of Physics and Astronomy, Northwestern University, Evanston, IL 60208, USA
[43] Remote Sensing Department, The Aerospace Corporation, 2310 E. El Segundo Blvd., El Segundo, CA 90245, USA

Abstract

The HR 2562 system is a rare case where a brown dwarf companion resides in a cleared inner hole of a debris disk, offering invaluable opportunities to study the dynamical interaction between a substellar companion and a dusty disk. We present the first ALMA observation of the system as well as the continued Gemini Planet Imager monitoring of the companion's orbit with six new epochs from 2016 to 2018. We update the orbital fit, and in combination with absolute astrometry from GAIA, place a 3σ upper limit of 18.5 M_J on the companion's mass. To interpret the ALMA observations, we used radiative transfer modeling to determine the disk properties. We find that the disk is well resolved and nearly edge-on. While the misalignment angle between the disk and the orbit is weakly constrained, due to the short orbital arc available, the data strongly support a (near) coplanar geometry for the system. Furthermore, we find that the models that describe the ALMA data best have inner radii that are close to the companion's semimajor axis. Including a posteriori knowledge of the system's SED further narrows the constraints on the disk's inner radius and places it at a location that is in reasonable agreement with (possibly interior to) predictions from existing dynamical models of disk truncation by an interior substellar companion. HR 2562 has the potential over the next few years to become a new test bed for dynamical interaction between a debris disk and a substellar companion.

Unified Astronomy Thesaurus concepts: Debris disks (363); Substellar companion stars (1648); Brown dwarfs (185); Orbit determination (1175); Gravitational interaction (669)

1. Introduction

Debris disks are the gas-poor disk structures surrounding stars as the outcome of the star formation process. The presence of a debris disk suggests that there is a need for larger bodies colliding and grinding down the dust grains in order to sustain the disk. Furthermore, observable features like gaps and warps in disk morphology can be the results of the dynamical interaction between a substellar companion and the disk itself. These features provide another pathway for us to find and study the properties of these potential planets residing near the disk. The most readily available example of this would be our Solar System, where substructures within the Asteroid Belt and the Kuiper Belt were created from the resonance between the planets' orbits and smaller objects (e.g., Tsiganis 2010). A great amount of information can be extracted from studying the dynamical interactions that would create such features in morphology in disk structures, even in the case where the companions are not directly detected. Sophisticated dynamical models have been developed to constrain properties of the companion from the properties of the disk and the system.

However, it is in fact difficult to find appropriate systems to test these models. Many of the currently discovered debris disks often do not have the required resolution to study the disk structures, and in those resolved disks, the detected companions are often found too far away from the disruption site to be solely responsible. Out of the systems where a companion is detected close to the irregular structure of the disk, there often is not convincing evidence for disk–companion interaction. As of today, only a few systems have been discovered to be candidates for disk–companion interaction. The first one of this kind is β Pictoris, a system with an almost perfectly edge-on debris disk with a vertical warp at 85 au, and a planet β Pictoris b that is consistent with this warp (Smith 1987; Augereau et al. 2001; Lagrange et al. 2009, 2010). It is believed that the inner warp of the disk is a result of the dynamical interaction between the planet β pic b and the disk, but studying this interaction is difficult due to the radial density profile being model-dependent (Augereau et al. 2001; Dawson et al. 2011). Only a handful of similar systems were discovered in the decades following the discovery of β Pictoris. Those systems all have potential dynamically interacting planets/brown dwarf candidates residing within the disks rings—but all of them lack determining

pieces of evidence, due to observational limitations or other possible scenarios for the disk structure formation (Su et al. 2017; Chauvin et al. 2018; Wilner et al. 2018; Musso Barcucci et al. 2019; Wang et al. 2021).

So far, only two systems have directly imaged brown dwarf companions orbiting inside the debris ring: HD 206893 (Marino et al. 2020; Nederlander et al. 2021) and HR 2562. In the former, it is unclear how close the companion is to the disk and whether it is responsible for truncating it. In this paper, we focus on analyzing the potential for dynamical interaction in HR 2562. HR 2562 is an F5V star with a mass of $1.3 M_\odot$, located at 34pc away from the Sun (Gray et al. 2006; van Leeuwen 2007a; Casagrande et al. 2011). Its debris disk was first imaged by Herschel (Moór et al. 2006). In 2016, Konopacky and the GPI team were able to directly image and obtain data for the orbit of the substellar companion, HR 2562 B, residing within the inner hole of the disk with GPIES. The orbit of HR 2562 B was further monitored by VLT/SPHERE for 10 months from 2016 to 2017, providing support for a coplanar geometry (Maire et al. 2018), and its spectral type was characterized as T2-T3 by IFS and IRDIS of VLT/SPHERE (Mesa et al. 2018). By comparison to evolutionary models, Konopacky et al. (2016) estimated a mass of $30 \pm 15\, M_{\rm jup}$ for the companion, with the uncertainty dominated by the poorly constrained age of the system. However, concrete evidence for brown dwarf–disk interaction would require a determination of the inner radius of the disk, which the initial characterization of the disk was unable to constrain, due to limited angular resolution (Moór et al. 2015). This led to an uninformative upper limit of $\sim 0.24 M_\odot$ based solely on dynamical arguments (Konopacky et al. 2016). Continued monitoring of the orbit as well as better-resolved observation of the disk are required to better characterize the disk, derive evidence for dynamical interaction, and further constrain the properties of the companion.

In this paper, we present the new Atacama Large Millimeter/submillimeter Array (ALMA) observation of the HR 2562 system (Section 2.1) as well as the updated GPI observation of the companion (Section 2.2). We present the reduced ALMA image in Section 3.1, and discuss the companion orbit fit, the coplanar scenario, and the dynamical mass limit in Section 3.2. The Monte Carlo Markov Chain (MCMC) fit for the ALMA image and the analysis are detailed in Section 4, and further
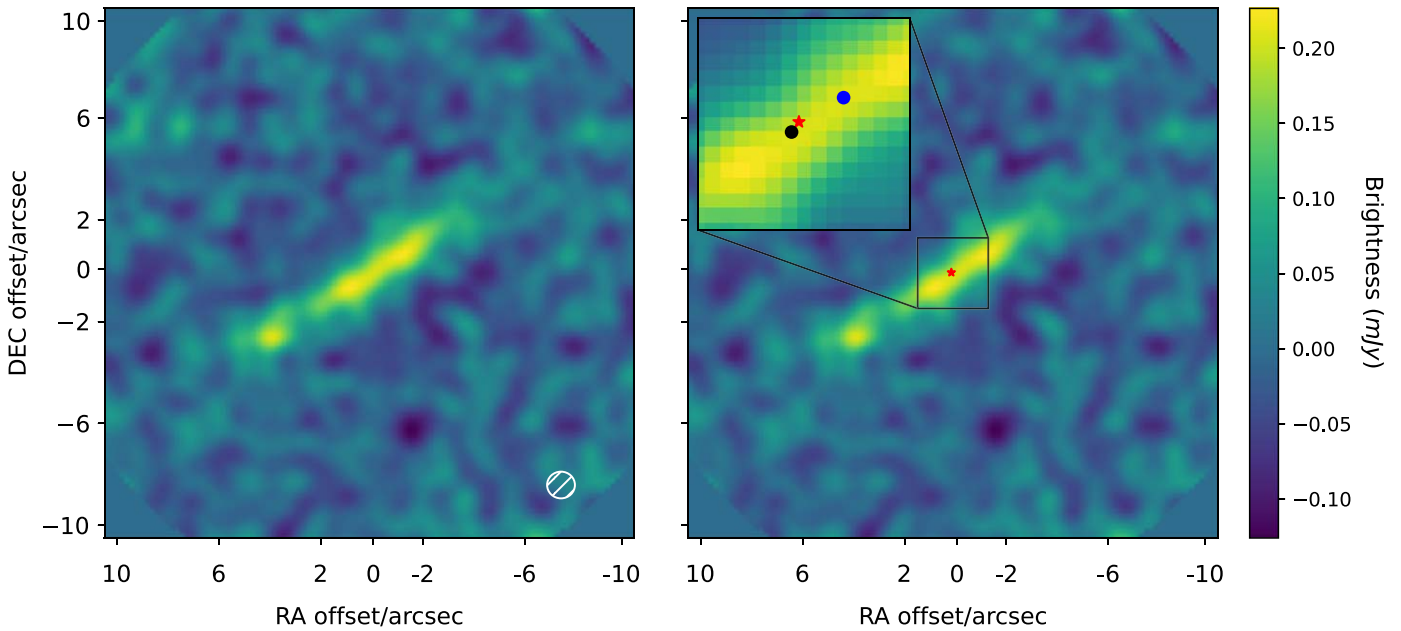
Figure 1. Left panel: ALMA data of the HR 2562 system at 870 μm. The (0,0) of the images correspond to R.A. = 102°.5, decl. = −60°.2; Right panel: a zoomed-in region of the center of the disk is shown in the top left corner. The black circle represents the center of the disk determined by 2D Gaussian fit, the red star represents the Gaia DR3 coordinates of the star HR 2562, and the blue circle represents the orbit-predicted location of the companion HR 2562 B on 2018 January 31st. The disk center and the star are well aligned, and the companion is close to the star as expected.

discussion on the system geometry, SED selection of the best-fitting models, and the dynamical interaction are presented in Section 5. We summarize our results and conclude in Section 6.

2. Observation

2.1. ALMA Observation

We observed the HR 2562 debris disk with the Atacama Large Millimeter Array (ALMA, project 2016.1.00880.S, PI: G. Duchêne) on 2018 May 15th. To maximize sensitivity for faint dust thermal emission in the system, we observed the target in Band 7 for a total on-source integration time of 37 minutes. Observing conditions were good, with 0.8 mm of precipitable water vapor at zenith. As a compromise between resolving the Herschel-estimated inner radius of the disk and minimizing spatial filtering on large scales, we selected configuration C40-1 with the 12 m array, with 44 antennas providing baselines ranging from 14 to 313 m and an angular resolution of about 1″.1. As this is a pure continuum observation, we used four 2 GHz bandwidth channels, centered at 336.5, 338.5, 348.5, and 350.5 GHz. Observations in all four bands are ultimately combined in a single continuum map at an effective frequency of 343.5 GHz (870 μm).

The data were processed with standard routines from the Common Astronomy Software Applications (CASA, McMullin et al. 2007), version 5.3.0–143. Specifically, we applied phase, bandpass, and flux calibrations using the provided calibrators. To produce the final continuum map, we used the task *tclean* with Briggs weighting with robust = 0.5. This results in a beam size of 1″.10 × 1″.06 at a position angle of −132°.3 and a rms of 0.0323 mJy beam^{-1}. The left panel of Figure 1 shows the final ALMA map generated with a 0″.2 pixel scale.

2.2. GPI Observation

2.2.1. Observations and Initial Reduction

The Gemini Planet Imager (GPI; Macintosh et al. 2014) is an instrument equipped with a high-order adaptive optics (AO) system (Poyneer et al. 2014, 2016), an apodized Lyot coronagraph (Soummer et al. 2011), and both a dispersing and a Wollaston prism for spectroscopic and polarimetric observations. The instrument was designed to achieve high contrast at small angular separations, providing sensitivity to substellar companions and circumstellar material around nearby, bright stars. HR 2562 was observed with GPI on 11 separate epochs between 2016 and 2018 under program IDs GS-2015B-Q-501 and GS-2017B-Q-501. The first four epochs were originally analyzed and published in Konopacky et al. (2016), but they are re-reduced and analyzed here to ensure consistency. The observing strategy was similar for each data set. The target was observed with GPI's coronagraphic mode with the specific coronagraph optimized for the near-infrared filter being used. After the coronagraph, a lenslet array and dispersing prism were used to disperse the light at each point within the 2″.8 × 2″.8 field into a low-resolution ($R \sim 35$–80) spectrum. The resulting dispersed field was imaged with GPI's integral field spectrograph (IFS; Chilcote et al. 2012; Larkin et al. 2014). In each data set, the star itself was used as the AO guide star. The observations were timed to be taken close to the meridian passage of the star over the observatory to maximize field rotation, ΔPA, for angular differential imaging (ADI; Marois et al. 2006). Observations of an argon lamp were taken during the target acquisition to measure the instrument flexure induced by the changing gravity vector as the telescope changes position. Standard dark and wavelength calibration frames were taken during the daytime as a part of the observatory's calibration plan. Table 1 provides a summary of the observations.

Table 1
HR 2562 Gemini/GPI Observing Log and Associated KLIP Parameters

UT Date	Filter	N_{exp}	t_{int} (s)	ΔPA[b] (°)	$\lambda_{min}-\lambda_{max}$[c] ($\mu$m)	n_λ[d]	m[e] (px)	n_{KL}[f]
2016 Jan 25[a]	H	33	59.6	19.4	1.514–1.778	35	3	5
2016 Jan 28[a]	K_1	21	59.6	10.6	1.947–2.173	26	3	5
2016 Jan 28[a]	K_2	20	59.6	10.5	2.119–2.226	15	3	5
2016 Feb 25[a]	K_2	43	59.6	25.7	2.116–2.224	15	3	5
2016 Feb 28[a]	J	53	59.6	26.6	1.137–1.330	35	3	5
2016 Dec 17	K_1	85	59.6	40.7	1.940–2.173	26	4	5
2017 Feb 13	H	19	59.6	12.3	.507–1.778	35	3	5
2017 Nov 29	H	50	59.6	30.1	1.511–1.773	35	3	5
2018 Jan 31	K_2	54	88.7	32.9	2.113–2.228	15	4	5
2018 Mar 10	Y	66	59.6	42.0	0.957–1.132	35	3	5
2018 Nov 19	H	24	59.6	12.5	1.509–1.779	35	3	5

Notes.
[a] Re-reduction of observations presented in Konopacky et al. (2016).
[b] Total field rotation over the duration of the observing sequence.
[c] Full spectral range used in the data reduction.
[d] Number of independent spectral channels.
[e] Minimum rotation-induced displacement for inclusion in the PSF subtraction process.
[f] Number of KLIP modes used in the PSF subtraction process.

The raw and associated calibration data were reduced through two separate processes. The raw data were reduced using the GPI Data Reduction Pipeline (DRP; Perrin et al. 2014) v1.5.0 revision `cafd46a`. This version of the pipeline resolved several issues identified with the calculation of the average parallactic angle during an exposure (De Rosa et al. 2020c). Although the magnitude of this correction was small for the data sets presented in Konopacky et al. (2016), between 0°.09 and 0°.12 (see Figure 17 in De Rosa et al. 2020c), we took the opportunity to reprocess these data along with the new epochs presented in this work. The data were reduced using the procedure outlined in De Rosa et al. (2020b). Briefly, the raw images were dark subtracted, and bad pixels were identified and replaced using a combination of a static bad pixel map and outlier rejection. The microspectra within each image were extracted to create a three-dimensional (x, y, λ) data cube containing the low-resolution spectra at each point within the field of view. Additional bad pixel identification was performed using outlier rejection. Distortion and anamorphism was corrected using a static distortion map applied to each slice within the data cube. The position and brightness of the star within each slice of each reduced data cube was estimated by measuring the four satellite spots generated by a wire diffraction grid within the pupil plane (Sivaramakrishnan & Oppenheimer 2006). The calibration data used to reduce the science data were not affected by the pipeline changes described in De Rosa et al. (2020c). We used the dark frames and wavelength calibrations generated by the GPIES Data Cruncher (Wang et al. 2018) created using v1.4.0 of the pipeline to reduce the science data, rather than reprocessing them with the updated pipeline.

2.2.2. PSF Subtraction and Astrometry

Although GPI can routinely achieve high Strehl ratios on bright stars, it does not offer perfect suppression of starlight. Within about 1″, the images are dominated by residual quasi-static speckles caused by AO fitting errors and non-common path aberrations. This residual light often has a pronounced azimuthal asymmetry in the direction of the jet stream (Madurowicz et al. 2018), which can result in a significant azimuthal dependence on the achieved contrast. We took advantage of both ADI and spectral differential imaging SDI, (Smith 1987; Racine et al. 1999) to subtract these quasi-static speckles from each slice within each data cube. We used `pyKLIP` (Wang et al. 2015), a Python implementation of the Karhunen–Loève image projection algorithm (KLIP; Soummer et al. 2012; Pueyo et al. 2015), to model and subtract the residual starlight within each image. Due to the distorting effects of this algorithm on the PSF of the companion within the PSF-subtracted image, we used the forward-model-based Bayesian KLIP-FM astrometry package (BKA; Wang et al. 2016) to model the effect of KLIP on the PSF of the companion (see Figure 2). We used the average of the four satellite spots as the instrumental PSF, and low-throughput channels were excluded.

We used the same approach for the BKA forward modeling as in De Rosa et al. (2020b). The PSF subtraction and forward model were calculated within a single annulus centered on the star with a width of either 16 px (Y, J, H) or 20 px (K_1, K_2). The radius of the annulus was selected to center the companion between the inner and outer edges. We explored the effect of varying two of the main tunable parameters: the movement criteria, m, that defines the minimum number of pixels an astrophysical source needs to have moved by before an image can be included within the reference PSF library, and the number of KL modes, n_{KL}, used to reconstruct the stellar PSF. We measured astrometry using BKA for each combination of these parameters. The forward model of the PSF was compared to the companion within a small 11×11 px box (15×15 px for K_1 and K_2). Posterior distributions of the position and flux of the companion, as well as the correlation length scale (a nuisance parameter to marginalize over), were sampled using the Markov Chain Monte Carlo (MCMC) affine-invariant sampler within the `emcee` package (Foreman-Mackey et al. 2013). We advanced 100 walkers that were initialized near the expected parameter values for 1000 steps, discarding the first 200 as burn-in.
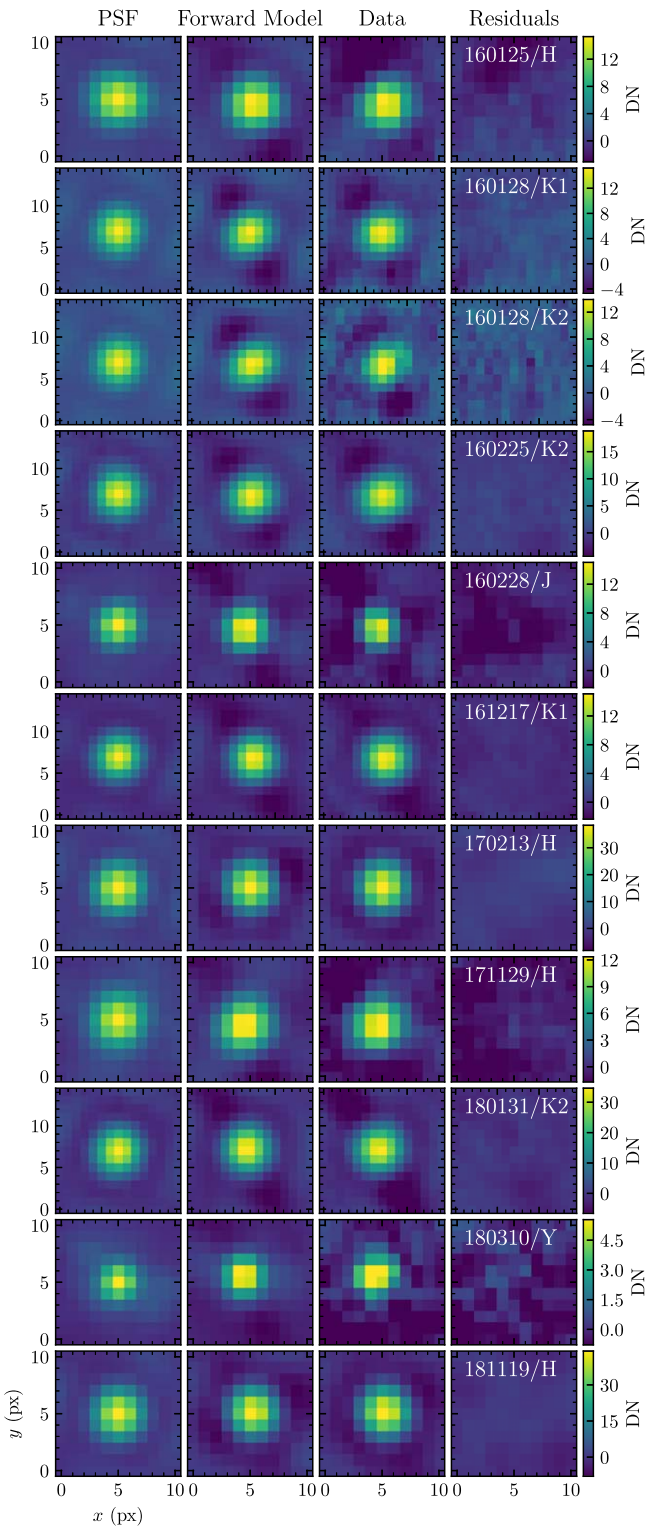
Figure 2. The GPI PSF estimated from the four satellite spots (left column), the BKA forward model (second column), the GPI images of HR 2562 B (third column), and the residuals (fourth column) for each observation. The color scales are different for each data set and are denoted by the color bar on the right. The KLIP parameters used for each reduction are given in Table 1.

Using this set of measurements, we investigated the effect of the KLIP parameters on the companion astrometry. Small values of m and large values of n_{KL} can cause significant self-subtraction or oversubtraction of the companion, an effect most pronounced at the longer wavelengths where the PSF is larger.

We found a significant correlation between these two parameters and the position of the companion for the two K_2 data sets, most pronounced in the 2018 January 31 epoch. For the other epochs at shorter wavelengths, no significant correlation was observed. The adopted KLIP parameters are listed in Table 2. A low value of n_{KL} was adopted, given the relative brightness of the companion, along with a high value of m to minimize self-subtraction, especially at longer wavelengths. The posterior distributions of the companion position measured using the adopted parameter set were combined with the instrument plate scale and orientation calibrations from De Rosa et al. (2020c) to yield on-sky relative astrometric measurements for each epoch (Table 2). An image of the instrumental PSF, forward model, companion, and residuals are shown for each data set in Figure 2.

3. Result

3.1. ALMA Image

As shown in Figure 1, the disk is clearly detected and well resolved along the major axis at 870 μm. Placing a beam-sized aperture around the brightest pixel in the image, we evaluate a peak signal-to-noise ratio of ∼7 in the ALMA image. Owing to spatial filtering by the interferometer, the reconstructed image has negative pixels surrounding the disk. This makes it difficult to measure the total flux of the disk directly from the ALMA image. To correct for this, we instead report a total flux of 3.3 mJy from integrating the best-fit model image (see Section 4.1). These observations extend the system's SED to a longer wavelength than all prior observations, most notably beyond the range of Herschel. With an angular resolution that is ≈6 times higher than Herschel's, the disk geometry is much more clearly apparent than in previous studies (Moór et al. 2015). The highly elongated structure reveals the disk to be nearly edge-on. Fitting a 2D Gaussian to the map results in an FWHM of 8."17 along the major axis and 0."97 along the minor axis of the disk. The aspect ratio of the two corresponds to an inclination of ≈83°, assuming a thin disk. We notice that the FWHM of the minor axis is marginally smaller than the size of the beam, indicating the disk is unresolved along the minor axis. Therefore, the ≈83° inclination we inferred from the aspect ratio is a strict lower limit.

To verify the alignment between the detected emission and the location of the star, we use the absolute astrometry information of the ALMA map, which is known to a precision of about 0."1 based on the pointing calibration. The position of the star is retrieved from the Gaia EDR3 Release, taking into account its proper motion and the epoch of the ALMA observation (Gaia Collaboration et al. 2021). The star and the center of the disk, as defined by our 2D Gaussian fit, are within 0."07 of each other, i.e., consistent with a symmetric disk about the star (see Figure 1). The location of the star and the center of the disk are shown in right panel of Figure 1.

From the image, a clump-like structure can be observed in the southeast side of the disk. This clump also manifests in the surface brightness profile of the disk shown in Figure 3, where we see a peak between 2″ and 6″. We show a horizontally flipped profile in dashed line in Figure 3, from which we can see that the peak stands at a marginally significant (∼2.5σ) difference as measured from the height of the brightness profile at the horizontally reflected location of the peak. There are a few plausible explanations for this feature: (1) It is due to the

Table 2
Relative Astrometry between HR 2562 A and HR 2562 B

UT Date	MJD	Instrument	Filter	Plate Scale (mas px^{-1})	North Offset (deg)	ρ (mas)	θ (deg)	References
2016 Jan 25	57412.1335	Gemini-S/GPI	H	14.161 ± 0.021	0.21 ± 0.23	615.05 ± 1.76	297.83 ± 0.27	1
2016 Jan 28	57415.1731	Gemini-S/GPI	K_1	14.161 ± 0.021	0.21 ± 0.23	612.56 ± 1.46	297.76 ± 0.25	1
2016 Jan 28	57415.2002	Gemini-S/GPI	K_2	14.161 ± 0.021	0.21 ± 0.23	613.47 ± 1.28	298.09 ± 0.24	1
2016 Feb 25	57443.0343	Gemini-S/GPI	K_2	14.161 ± 0.021	0.21 ± 0.23	616.09 ± 1.23	297.71 ± 0.24	1
2016 Feb 28	57446.0951	Gemini-S/GPI	J	14.161 ± 0.021	0.21 ± 0.23	616.44 ± 1.37	297.78 ± 0.25	1
2016 Dec 12	57734.2647	VLT/SPH-IRD	H	12.251 ± 0.009	-1.808 ± 0.043	637.80 ± 6.40	297.81 ± 0.54	2
2016 Dec 17	57739.3123	Gemini-S/GPI	K_1	14.161 ± 0.021	0.32 ± 0.15	639.89 ± 1.27	297.98 ± 0.17	1
2017 Feb 7	57791.1114	VLT/SPH-IRD	H	12.251 ± 0.009	-1.712 ± 0.058	644.00 ± 2.30	297.82 ± 0.19	2
2017 Feb 13	57797.0517	Gemini-S/GPI	H	14.161 ± 0.021	0.32 ± 0.15	644.20 ± 1.22	298.23 ± 0.16	1
2017 Sep 29	58025.3826	VLT/SPH-IRD	K_1	12.267 ± 0.009	-1.735 ± 0.043	661.20 ± 1.30	297.97 ± 0.16	2
2017 Sep 29	58025.3826	VLT/SPH-IRD	K_2	12.263 ± 0.009	-1.735 ± 0.043	658.90 ± 1.60	298.08 ± 0.17	2
2017 Nov 29	58086.3110	Gemini-S/GPI	H	14.161 ± 0.021	0.28 ± 0.19	664.82 ± 2.04	298.37 ± 0.24	1
2018 Jan 31	58149.1962	Gemini-S/GPI	K_2	14.161 ± 0.021	0.28 ± 0.19	669.44 ± 1.24	298.55 ± 0.20	1
2018 Mar 10	58187.0475	Gemini-S/GPI	Y	14.161 ± 0.021	0.28 ± 0.19	670.84 ± 2.83	298.74 ± 0.26	1
2018 Nov 19	58441.3261	Gemini-S/GPI	H	14.161 ± 0.021	0.45 ± 0.11	685.76 ± 1.25	298.89 ± 0.13	1

Note.
References. (1) This work; (2) Maire et al. 2018.

random noise of the image. (2) The trough is a real feature that represents a real physical underdensity, e.g., a gap or spiral in the disk, thus making the disk asymmetrical. (3) The trough is the result of a contamination from an unrelated point source, presumably a background submillimeter galaxy. While a physical disk origin cannot be ruled out, the signal-to-noise ratio means we cannot say with confidence that the feature is real. In addition, although it is possible that there might be previously unseen background galaxy, the chance of it aligning so well with the disk is low. We will therefore model the disk with a symmetric profile in the analysis that follows, but note that future observations may better determine the nature of the trough.

3.2. Orbit of the Brown Dwarf Companion

3.2.1. Unconstrained Fit

The orbit of the companion was fitted to the measured astrometry in Table 2 using a modified version of the procedure described in De Rosa et al. (2020b). The visual orbit can be described using the standard Campbell elements: the period (P), semimajor axis (a), eccentricity (e), inclination (i), argument of periastron (ω), position angle of the ascending node (Ω), and the time of periastron (T_0). Here, we use the standard convention that Ω refers to the position angle that the companion passes through the plane tangent to the sky at the location of HR 2562, moving away from the observer. We substituted two of these elements when fitting the orbit of HR 2562. P was replaced with the total system mass ($M_{\rm total}$), as the period is currently unconstrained given the measurements, and T_0 was replaced with the dimensionless parameter τ describing the time of the next periastron passage in fractions of the orbital period since MJD 57412.1335, the start of the astrometric record. In addition to these seven elements, we also required the distance to the star, represented by the parallax (ϖ), in order to link the angular semimajor axis to the system mass to derive the orbital period.

We used the parallel-tempered affine-invariant MCMC sampler within the `emcee` package (Foreman-Mackey et al. 2013) to
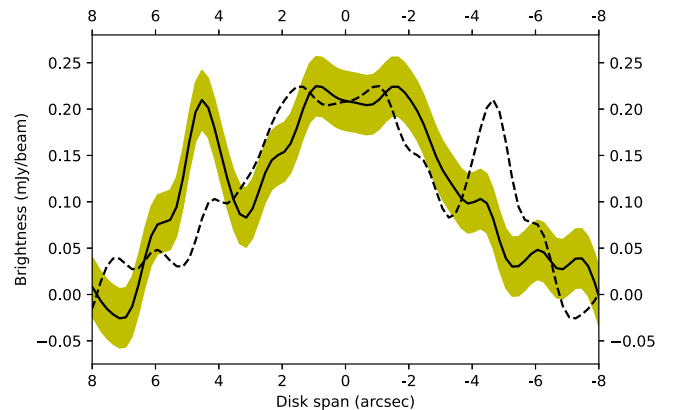

Figure 3. 870 μm brightness profile along the disk major axis. The yellow shade indicates the 1σ uncertainty as determined from the surrounding background areas. The dashed line represent a horizontally reflected brightness profile about the location of the star.

sample the posterior distribution of these eight parameters describing the visual orbit of HR 2562 B. We performed the sampling using the parameters $\log a$ and $\cos i$ to enforce a log-uniform prior probability density function (PDF) on a and a sine prior PDF on i, rather than computing the prior probability at each step. Gaussian priors were used for $M_{\rm total}$ ($1.31 \pm 0.13\, M_\odot$; Moór et al. 2015), under the assumption that $M_2 \ll M_1$, and ϖ (29.4738 ± 0.0185 mas; Gaia Collaboration et al. 2021). We advanced 512 chains at each of 16 different temperatures for one million steps. In the parallel-tempered framework the lowest-temperature chains sample the posterior probability distribution, while the highest-temperature chains sample the prior probability distribution. We saved every hundredth sample of each chain to disk, and conservatively discarded the first half of each as a "burn-in."

Table 3, along with the set of parameters describing the maximum likelihood (minimum χ^2) and maximum probability orbit. A random selection of visual orbits consistent with the relative astrometry are shown in Figure 4. The posterior PDFs for a subset of the fitted and derived parameters are shown in Figure 5

Table 3
Orbital Elements for HR 2562 B

Parameter	Unit	Visual			Visual + Prior			Visual + Absolute		
		Range	max. $\mathcal{L}$	max. $\mathcal{P}$	Range	max. $\mathcal{L}$	max. $\mathcal{P}$	Range	max. $\mathcal{L}$	max. $\mathcal{P}$
Fitted Parameters										
$\log a$	[arc sec]	$-0.305^{+0.180}_{-0.078}$	-0.286	-0.401	$-0.170^{+0.112}_{-0.099}$	-0.343	-0.260	$-0.252^{+0.115}_{-0.116}$	-0.234	-0.204
$\cos i$	$\cdots$	$0.165^{+0.306}_{-0.073}$	0.110	0.531	$0.098^{+0.020}_{-0.017}$	0.131	0.114	$0.125^{+0.211}_{-0.036}$	0.089	0.103
e	$\cdots$	$0.79^{+0.18}_{-0.35}$	0.58	0.98	$0.29^{+0.28}_{-0.21}$	0.67	0.52	$0.63^{+0.32}_{-0.23}$	0.45	0.55
ω	deg	$202.2^{+42.7}_{-26.6}$	210.4	186.2	$179.8^{+69.1}_{-17.3}$	182.5	170.9	$207.2^{+34.6}_{-30.1}$	216.5	230.9
Ω	deg	$299.2^{+3.1}_{-3.8}$	298.7	298.0	$302.1^{+0.8}_{-0.8}$	300.5	302.3	$299.5^{+2.5}_{-2.7}$	299.3	298.5
τ	$\cdots$	$0.794^{+0.079}_{-0.040}$	0.780	0.785	$0.696^{+0.078}_{-0.089}$	0.716	0.685	$0.795^{+0.075}_{-0.057}$	0.785	0.841
ϖ	mas	$29.474^{+0.018}_{-0.018}$	29.464	29.476	$29.474^{+0.018}_{-0.018}$	29.463	29.473	$29.474^{+0.018}_{-0.018}$	29.507	29.474
$M_{\rm Total}$	$M_\odot$	$1.34^{+0.13}_{-0.12}$	1.67	1.33	$1.34^{+0.12}_{-0.12}$	1.67	1.37	$\cdots$	$\cdots$	$\cdots$
M_1	$M_\odot$	$\cdots$	$\cdots$	$\cdots$	$\cdots$	$\cdots$	$\cdots$	$1.34^{+0.13}_{-0.12}$	1.44	1.36
$\log M_2$	$[M_{\rm Jup}]$	$\cdots$	$\cdots$	$\cdots$	$\cdots$	$\cdots$	$\cdots$	$-0.40^{+1.14}_{-1.07}$	1.07	1.01
$\Delta\alpha^\star$	mas	$\cdots$	$\cdots$	$\cdots$	$\cdots$	$\cdots$	$\cdots$	$0.59^{+0.66}_{-0.43}$	1.90	1.75
$\Delta\delta$	mas	$\cdots$	$\cdots$	$\cdots$	$\cdots$	$\cdots$	$\cdots$	$0.06^{+0.39}_{-0.51}$	-0.72	-0.48
$\Delta\mu_{\alpha^\star}$	mas yr^{-1}	$\cdots$	$\cdots$	$\cdots$	$\cdots$	$\cdots$	$\cdots$	$0.56^{+0.02}_{-0.11}$	0.35	0.37
$\Delta\mu_\delta$	mas yr^{-1}	$\cdots$	$\cdots$	$\cdots$	$\cdots$	$\cdots$	$\cdots$	$-0.46^{+0.06}_{-0.02}$	-0.35	-0.36
σ_Λ	mas	$\cdots$	$\cdots$	$\cdots$	$\cdots$	$\cdots$	$\cdots$	$2.35^{+0.26}_{-0.24}$	2.23	2.25
Derived Parameters										
P	yr	$60.1^{+51.2}_{-14.7}$	56.8	42.9	$95.4^{+45.1}_{-28.6}$	46.8	68.8	$71.5^{+35.7}_{-23.2}$	72.9	83.5
a	arc sec	$0.496^{+0.255}_{-0.082}$	0.517	0.397	$0.676^{+0.198}_{-0.138}$	0.454	0.549	$0.560^{+0.169}_{-0.131}$	0.583	0.625
a	au	$16.8^{+8.7}_{-2.8}$	17.6	13.5	$22.9^{+6.7}_{-4.7}$	15.4	18.6	$19.0^{+5.7}_{-4.4}$	19.8	21.2
$r_{\rm apo}$	au	$28.8^{+8.4}_{-1.9}$	27.7	26.6	$29.3^{+3.3}_{-1.5}$	25.7	28.4	$29.2^{+7.2}_{-2.1}$	28.6	32.9
i	deg	$80.5^{+4.2}_{-18.6}$	83.7	57.9	$84.4^{+1.0}_{-1.2}$	82.5	83.5	$82.8^{+2.0}_{-12.5}$	84.9	84.1
T_0	yr	$2005.0^{+1.6}_{-4.9}$	2003.5	2006.8	$1991.0^{+7.6}_{-20.2}$	2002.8	1994.4	$2003.3^{+2.9}_{-6.1}$	2000.4	2002.8
M_2	$M_{\rm Jup}$	$\cdots$	$\cdots$	$\cdots$	$\cdots$	$\cdots$	$\cdots$	<18.5	11.67	10.28
Goodness of Fit										
χ^2_ρ	$\cdots$	$6.79^{+2.96}_{-1.66}$	3.54	4.34	$10.61^{+3.19}_{-2.49}$	3.92	7.91	$6.88^{+3.00}_{-1.71}$	4.23	4.21
χ^2_θ	$\cdots$	$17.84^{+2.28}_{-1.03}$	16.48	16.46	$17.80^{+2.17}_{-1.00}$	16.70	16.47	$17.83^{+2.27}_{-1.03}$	17.07	17.49
$\chi^2_{\rm HIP}$	$\cdots$	$\cdots$	$\cdots$	$\cdots$	$\cdots$	$\cdots$	$\cdots$	$108.4^{+14.8}_{-13.6}$	111.1	110.2
$\chi^2_{\rm Gaia-Pos.}$	$\cdots$	$\cdots$	$\cdots$	$\cdots$	$\cdots$	$\cdots$	$\cdots$	$1.84^{+1.85}_{-1.20}$	0.10	0.01
$\chi^2_{\rm Gaia-PM}$	$\cdots$	$\cdots$	$\cdots$	$\cdots$	$\cdots$	$\cdots$	$\cdots$	$1.40^{+2.30}_{-1.05}$	0.01	0.08
χ^2_ν	$\cdots$	$1.15^{+0.17}_{-0.11}$	0.91	0.95	$1.32^{+0.17}_{-0.13}$	0.94	1.11	$1.11^{+0.12}_{-0.11}$	1.06	1.06

Notes. Orbits with $\Omega < 180°$ were wrapped by $\omega + 180$, $\Omega + 180$, τ in fractions of the orbital period since MJD 57412.1335. Reduced χ^2 calculated using 22° of freedom for the visual orbit fit, and 125 for the combined fit.

(black contours). We found a strong anticorrelation between the eccentricity and the inclination of the orbit; less eccentric orbits tend to have a more edge-on configuration ($i \sim 84°$). Although very high eccentricities are seemingly preferred based on the shape of the PDF, the eccentricity of the orbit is not yet constrained well and is still dependent on the input priors. We discuss this further in Section 3.2.4.

3.2.2. Coplanar Scenario

The results regarding the orbit of the companion presented so far make no assumptions regarding the alignment of the orbital plane with that of the debris disk resolved in the ALMA observations presented in Section 2.1. We repeated the orbit-fitting procedure described above with an additional prior on the inclination (i) and position angle of the ascending node (Ω) to investigate the properties of orbits consistent with both the measured astrometry and a near-coplanar configuration with respect to the external debris disk. We used Gaussian kernel density estimation (KDE) to construct a prior probability density function on the orbital inclination (i) and position angle (Ω) from the disk fitting MCMC samples (Section 4). We used the scipy.Gaussian_kde function with Scott's method for the estimator bandwidth calculation. The resulting two-dimensional prior distribution is shown in Figure 6, along with the two marginalized distributions. The Gaussian KDE is a good match to the posterior distributions describing the disk geometry from the ALMA observations presented in Section 4. The additional term in the prior probability was calculated using the Gaussian KDE and the value of i and Ω at each step in the MCMC process. We accounted for the ambiguity in these two parameters when fitting to the ALMA data by evaluating the Gaussian KDE at four possible combinations of i and Ω: (i, Ω), $(i, \Omega + \pi)$, $(\pi - i, \Omega)$, and $(\pi - i, \Omega + \pi)$. The maximum of these four values was used as the prior probability at this step for this combination of i and Ω.

The median and 1σ credible intervals for the posterior distributions on the fitted and derived parameters from this analysis are given in Table 3, in addition to the maximum
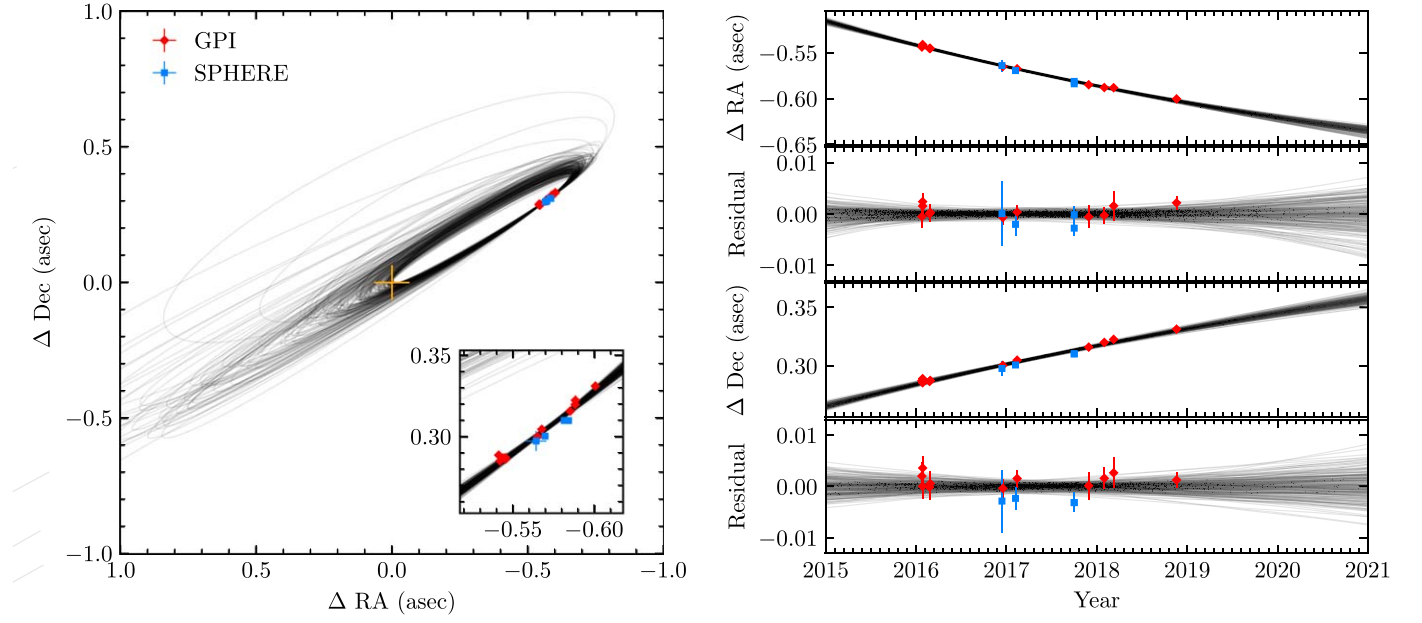
Figure 4. (left panel) Relative astrometry of HR 2562 B relative to HR 2562 from GPI (red) and SPHERE (blue). The location of the host star is indicated by the orange cross. Two hundred orbits drawn from the MCMC analysis (black curves) are also shown. (right panel) Offset between HR 2562 and the companion, and the residual compared with the median orbit, in the R.A. (top) and decl. (bottom) directions.
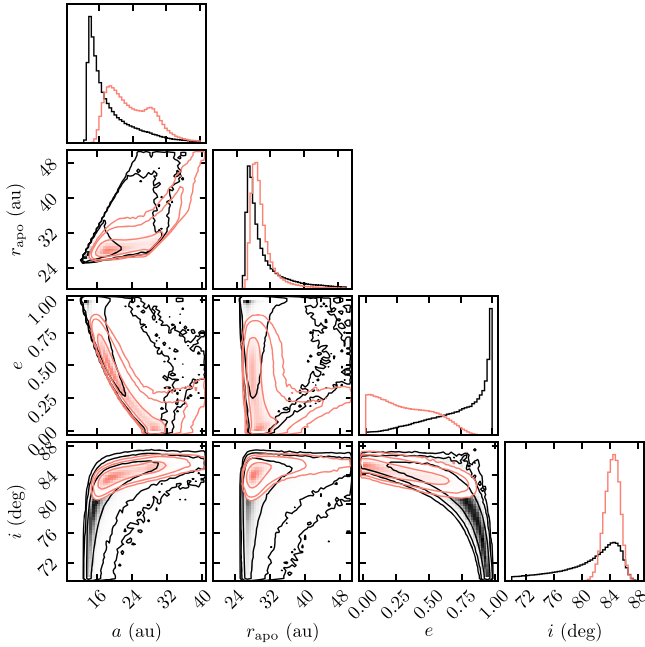

Figure 5. Posterior distributions and associated covariances of the semimajor axis (a), periastron distance (r_{apo}), eccentricity (e), and inclination (i) from an orbit fit with (red) and without (black) a prior probability on the inclination and position angle (Ω) derived from the ALMA disk fitting. Contours represent the 1σ, 2σ, and 3σ confidence levels. Limiting the orbit to a coplanar configuration removes the tail of extremely high-eccentricity orbits.

Figure 6. Normalized joint prior probability on the orbital inclination i and position angle Ω estimated using a Gaussian KDE for the coplanar scenario (main panel). Solid contours are spaced in 0.2 dex increments from -1.8 to -0.2; the inner dashed contour is at -0.01. Marginalized distributions are shown in the top and right panels for the posterior distribution estimated from the ALMA data (black solid histogram, Section 4) and for the prior distribution used in the orbit fit (red dashed histogram).

likelihood and maximum probability orbit. The posterior distributions of a subset of the fitted and derived parameters are compared to those calculated without the additional prior in Figure 5. The full corner plot is presented in Appendix B. The additional prior restricts the range of orbital eccentricities that are consistent with the measured astrometry in that very eccentric orbits ($e \gtrsim 0.8$) require increasingly misaligned configurations with respect to the outer disk when considering the general fit. The other orbital parameters are not significantly

affected by the prior; in particular, the apoastron distance is unchanged, due to the anticorrelation between the orbital eccentricity and semimajor axis.

3.2.3. Dynamical Mass Constraint

We used the relative astrometry between the star and companion presented here and absolute astrometric measurements of the photocenter from the Hipparcos and Gaia satellites

to constrain the mass of the companion. With a sufficiently high mass for the companion, the photocenter of the system will be perturbed from linear motion through space, due to the orbit of the star around the barycenter of the system. For Hipparcos, we used the intermediate astrometric data (IAD), i.e., the residuals along the scan direction from the best-fit astrometric solution (van Leeuwen 2007b). These astrometric measurements of HR 2562 were best fit with a nonstandard "stochastic" solution where the uncertainties on the individual measurements are inflated to reduce the goodness-of-fit statistic below an acceptable threshold for the final catalog (van Leeuwen 2007a). The need for this type of solution can be attributed to unresolved orbital motion on a timescale much shorter than the three-year duration of the mission, or to remaining modeling noise from the construction of the catalog (van Leeuwen 2007b).

For Gaia, we used the astrometric parameters and correlation coefficients reported in the Early Data Release 3 catalog (EDR3; Gaia Collaboration et al. 2021). We compared the various goodness-of-fit metrics reported in the EDR3 catalog for HR 2562 to those of stars with a similar brightness. As illustrated in Appendix A, HR 2562 appears relatively well behaved compared to these other sources. We also collected the timings of the individual Gaia measurements using the Gaia Observation Forecast Tool,[44] excluding those taken during satellite downtimes reported in Lindegren et al. (2021).

The procedure used in De Rosa et al. (2020a) for a joint fit of absolute astrometry and radial velocity measurements was adapted to fit the absolute and relative astrometric measurement available for HR 2562, in addition to updating it to account for the change in reference epoch between Gaia DR2 and EDR3. The model that simultaneously describes the orbit of the companion around HR 2562 and the orbit of the photocenter around the barycenter of the system consists of 14 parameters. Seven parameters are used in the orbit fit described in Section 3.2.1 ($\log a$, $\cos i$, e, ω, Ω, τ, and ϖ), two describe the masses of the components (M_1 and $\log M_2$), four describe offsets between the Hipparcos catalog astrometry and the barycenter position and proper motion at 1991.25 ($\Delta\alpha^\star$, $\Delta\delta$, $\Delta\mu_{\alpha^\star}$, and $\Delta\mu_\delta$), and one is an error inflation term applied in quadrature to the Hipparcos IAD (ϵ_Λ). To calculate the semimajor axis of the photocenter orbit, we used an empirical mass-magnitude relationship to determine the relative fluxes of the two components in the Hipparcos and Gaia passbands when $M_2 > 0.077\ M_\odot$ (Pecaut & Mamajek 2013). For lower masses, we assumed that the companion is emitting no flux, and that the photocenter is coincident with the location of the host star.

We used the same MCMC sampler as in Section 3.2.1 to sample the posterior distributions of the 14 parameters in this model. We used Gaussian priors for the parallax ($\varpi = 29.4738 \pm 0.0185$ mas) and for the mass of the primary ($M_1 = 1.31 \pm 0.13\ M_\odot$); uniform priors were used for the remaining parameters. We advanced 512 chains at each of 16 different temperatures for one million steps, saving every tenth sample to disk. The first half of each chain was discarded as a "burn-in."

The median and one-sigma confidence intervals for the fitted and derived parameters are shown in Table 3, along with the set of parameters describing the maximum likelihood and maximum probability orbit. The covariance between the
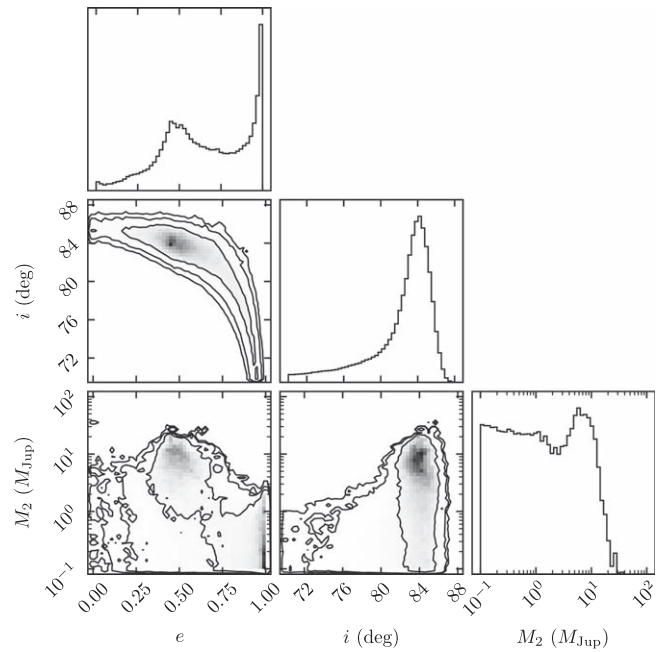
Figure 7. Posterior distributions and associated covariance of the orbital eccentricity (e), inclination (i), and companion mass (M_2) from a joint fit to the relative and absolute astrometry. Contours represent the 1σ, 2σ, and 3σ confidence intervals.

eccentricity, inclination, and mass of the companion is shown in Figure 7. The eccentricity and inclination exhibit an anticorrelation similar to that seen for the visual orbit fit (Figure 5), albeit with a slight enhancement of orbits with a moderate eccentricity ($e \sim 0.5$). The shape of the M_2 posterior probability distribution (Figure 7, lower right panel) clearly demonstrates that we do not yet have a statistically significant measurement of the mass of the companion. Instead, we can only place an upper limit of $M_2 < 18.5\ M_{\rm Jup}$ at the 99% confidence level, given our assumptions regarding the prior probability distribution. It should be noted that the exact number, while prior-dependent, is expected to be rather precise, given the sharp truncation of the posterior. Below this value, the posterior probability distribution is not significantly different from that of the prior probability distribution that was uniform in $\log M_2$. The proper motion of the HR 2562 photocenter between the Hipparcos and Gaia missions is shown in Figure 8. The proper motion measurements are consistent with companion masses $\lesssim 20\ M_{\rm Jup}$; higher-mass companions would have caused a larger-amplitude astrometric reflex motion between the two epochs, inconsistent with the observations.

3.2.4. The Case for Low-eccentricity Solutions

As shown here, the limited coverage of the companion's orbit still leaves a broad range of possible orbits. In short, the data are consistent with both low- to moderate-eccentricity orbits that are roughly coplanar with the debris disk as well as high-eccentricity orbits at a significantly different inclination. It is worth noting that, with such limited orbital phase coverage, Keplerian fits are notoriously subject to eccentricity and inclination biases (e.g., Lucy 2014; Ferrer-Chávez et al. 2021) and they remain highly sensitive to the MCMC priors (Pearce et al. 2015; O'Neil et al. 2019). These effects are highly sensitive to the exact orbital phase coverage and system viewing geometry, so they are hard to evaluate and correct for.
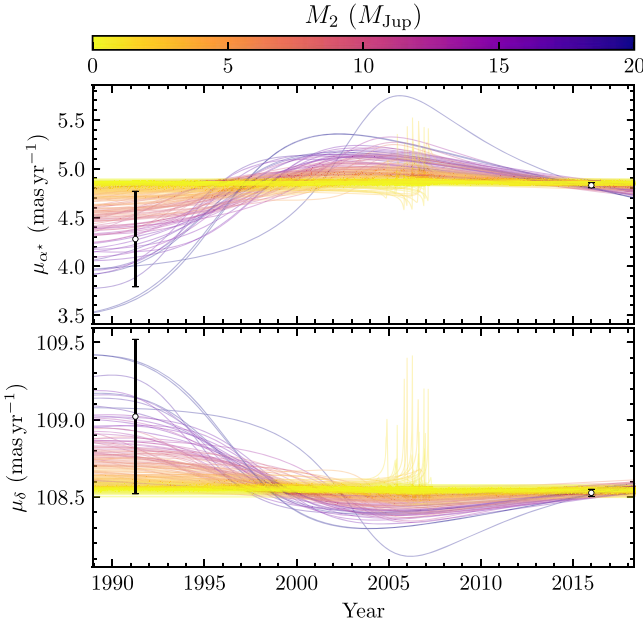
Figure 8. Apparent proper motion of the photocenter of the HR 2562 system in the R.A. (top) and decl. (bottom) directions for 200 orbits drawn from the MCMC analysis presented in Section 3.2.3 that are consistent with the absolute and relative astrometry. The tracks are colored by the mass of the companion for each orbit. The astrometric measurements from the Hipparcos and Gaia catalogs are plotted.

While only more extensive astrometric coverage will solve both issues, it is worth taking an holistic approach of the results presented here. In particular, a high-eccentric and misaligned companion would most likely result in an eccentric disk through apsidal alignment and/or a significant warp in the system. The ALMA map presented here does not provide strong evidence for either phenomenon, suggesting that a lower eccentricity and near coplanarity should be preferred.

As an additional test, we performed an orbital fit where we forced $e = 0$. The resulting fit is slightly poorer, with $\chi^2 = 21.9$ (to be compared with $\chi^2 = 20.0$ for the eccentric fit). Given 15 two-dimensional data points and six (eight) free parameters for the circular (eccentric) fit, both the Bayesian Information Criterion and the Aikake Information Criterion indicate that the data are fit sufficiently well by the circular fit. Since it is unlikely that the orbital is exactly circular, we will use the result of the full Keplerian fit in the remainder of this study, but we consider that both physical arguments and the circular fit provide suggestive evidence against the high-eccentricity orbital solutions.

4. Disk Modeling

4.1. Modeling Setup

We model the submillimeter emission from the disk with MCFOST, a radiative transfer code for circumstellar modeling (Pinte et al. 2006). In short, the system is set up as a central star surrounded by a circumstellar disk where the stellar radiation is propagated through the disk using a Monte Carlo process to evaluate the dust temperature in all locations, and the resulting thermal emission map is generated using a ray-tracing method. We assume that the disk is axisymmetric and that its dust population can be represented by a uniform composition (astronomical silicates from Draine & Lee 1984) and power-law size distribution. We assume an $N(a) \propto a^{-3.5}$ distribution

(Dohnanyi 1969) that extends from $3 \mu m$, the approximate blowout size for a mid-F star (e.g., Pawellek & Krivov 2015), to 1 mm. As is applicable for optically thin disks, the dust grains are assumed to be in radiative equilibrium with the stellar radiation field, but local thermal equilibrium is not enforced. This leads to the smaller dust grains being super-heated compared to large grains and to the blackbody approximation. The star emission is simulated using a 6600 K stellar spectrum generated by the PHOENIX grid, with a total luminosity of $3.1 L_\odot$ (see, e.g., Moór et al. 2015).

Following standard practice for debris disks (e.g., Augereau et al. 1999; Esposito et al. 2020), we select the following prescription for the disk density as a function of position between the disk's inner (R_{in}) and outer (R_{out}) radii:

$$\rho(r, z) \propto \left(\left(\frac{r}{R_c} \right)^{-2p_{in}} + \left(\frac{r}{R_c} \right)^{-2p_{out}} \right)^{-1/2}$$
$$\times \exp \left(-\left(\frac{|z|}{h(r)} \right)^{\gamma_{vert}} \right). \quad (1)$$

We fix $\gamma_{vert} = 1$ for an exponential vertical profile. The corresponding scale height, $h(r)$, is assumed to be a linear function of radius, i.e., the disk has a bow-tie shape. In this case, $h = h_0 \frac{r}{r_0}$ where r_0 is an arbitrary reference radius. We selected $r_0 = 100$ au. The surface density profile is a smoothly connected pair of power-law regimes, with exponents p_{in} and p_{out} at radii $r \ll R_c$ and $r \gg R_c$ if $p_{in} > 0$ and $p_{out} < 0$, as is usually the case. The peak surface density occurs near, but not exactly at, $r = R_c$, depending on the value of p_{in} and p_{out} (Augereau et al. 1999). The total dust mass, M_d, is obtained by integrating Equation (1) from the disk's inner and outer radii, R_{in} and R_{out}, respectively.

The disk image is then produced for a combination of inclination (i) and position angle (PA) with a pixel scale of $0\rlap{.}''2\,pixel^{-1}$, convolved with a 2D Gaussian beam constructed with the major and minor axes and the position angle from the ALMA beam. To reduce the issue of correlated noise in the interferometric map, we rebin the observed and model images to a $1''\,pixel^{-1}$ scale so that each pixel can be reasonably considered as independent of its neighbors. The two images are aligned based on the 2D Gaussian fit to the observed image and a χ^2 goodness-of-fit metric is computed based on a $20'' \times 20''$ field of view centered on the disk.

With this routine established, we proceed to perform a Monte Carlo Markov Chain (MCMC) run to determine the best-fit parameter for the disk. We vary a total of nine parameters: i, PA, M_d, R_c, R_{in}, R_{out}, p_{in}, p_{out}, h_0. The values of the priors are given in Table 4. The ensemble initializes the walkers with flat priors for every parameter except for the dust mass, which was sampled from a log-uniform prior. With these priors, we set up the two-temperature MCMC with 100 walkers both for the hot and cold chains. We ran the chain for 2000 iterations with a script adapted from *diskmc* (Esposito et al. 2018) and verified that the chain had reached convergence by the end of the run. The first 600 iterations were rejected as burn-in steps.

4.2. Results

The best-fit model and the associated residuals are presented in the top row of Figure 9. This model describes the data

Table 4
Disk Physical Parameters from ALMA Map Fitting

Parameter	Unit	Prior Range	Best Fit — ALMA	Confidence Interval	Best Fit —SED
M_d	$M_\oplus$	$(4.2 \times 10^{-5},$ $3.3 \times 10^5)$	0.0182	$0.0192^{+0.0016}_{-0.0015}$	0.0158
PA	°	(−60.,120.)	32.7	$32.7^{+0.7}_{-0.8}$	33.6
i	°	(0., 90.)	84.7	$\geqslant 79.3$	87.1
p_{out}		(−10., 0.)	−1.2	$-1.2^{+0.3}_{-0.4}$	−0.8
p_{in}		(0,10.)	3.05	$\leqslant 10.2$	7.6
R_c	au	(20.,150.),	41.0	$\leqslant 114.4$	47.6
R_{in}	au	(0.1, 75.)	20.3	$\leqslant 62.3$	34.0
R_{out}	au	(200.,401.)	260.0	$258.8^{+26.8}_{-21.2}$	234.3
h_0	au	(0.5., 20.)	1.58	$\leqslant 11.0$	3.91

Notes. We report the prior ranges, best-fit image parameter, the 1σ confidence interval, and the best-fit SED parameter. For less-constrained parameters, 3σ upper or lower limits are reported instead. The reference radius is set to $r_0 = 100$ au.

reasonably well ($\chi^2_{red} = 1.50$), with nearly random residuals—and in particular, no structured residuals at the location of the disk emission. Considering the entirety of the MCMC chain (Figure 10), we find that several parameters (PA, M_d, R_{out}, and p_{out}) are well constrained and we report their 1σ confidence intervals in Table 4. For the remainder of the parameters, we obtained 3σ upper (R_{in}, p_{in}, R_c, and h_0) or lower (i) limits from our posteriors. As expected, given that the disk is resolved well in our ALMA observations, several of the geometric parameters are well constrained. In addition, the disk mass is well constrained by the integrated flux of the disk.

The corner plot reveals important correlations between parameters. First of all, there is some ambiguity between the disk inclination and its vertical extent. In particular, the ALMA map is consistent with a vertically thin disk inclined at about 84°, but a thicker disk viewed almost exactly edge-on would also be consistent with the observations. This is unsurprising, given the ≈35 au linear resolution of these observations; higher-resolution mapping will be necessary to tighten the constraints on these parameters. The second correlation connects the disk radial extent and its surface density profile. For instance, higher values of R_c are associated with a steeper outer density profile. Furthermore, the inner disk radius and inner density profile slope have broad ranges of allowed values because the resolution of our ALMA observations does not allow us to fully resolve the disk inner hole. We place a 3σ upper limit on both parameters from the ALMA map and will further explore their relations with other available information in the next section.

5. Analysis

5.1. System Geometry

Since the discovery of the HR 2562 B substellar companion and the initial mapping of the disk structure with Herschel, the observations presented here have allowed us to further our understanding of the system: the continued imaging of the companion provides tighter constraints on its orbit, the Gaia DR3 release opens the door to a dynamical mass estimate on the brown dwarf via the absolute astrometry of the star, and the better-resolved ALMA data further clarify the geometric

structure of the disk. Most importantly, with the updated companion orbit and the resolved image of the disk, we are in a good position to quantify the system geometry and obtain concrete evidence of direct interaction between HR2562B and the debris disk.

We first focus on our updated constraints on the disk properties. A similar analysis was performed in Moór et al. (2015) to derive the properties of the disk. The acceptable ranges for the geometrical disk parameters are consistent between their study and our fit result, although R_{in} and R_{out} are less constrained by the Herschel observations, due to their lower resolution, which leads to the disk being only marginally resolved. To further contrast the ALMA observation with the Herschel observation, we recreate the Herschel best-fit model using MCFOST with the single power-law density profile and the best-fit parameters from Moór et al. (2015), and adjusting the dust mass so that the total flux of the disk model matches the measured SED of the system at 70 μm. The resulting image is then convolved with the PACS beam. We also produce the 70 μm image of the best-fit model to the ALMA data, again convolving it with the PACS beam. The comparison between observed and synthetic Herschel observations is presented in Figure 11. The Herschel disk looks geometrically similar to our best-fit result, as we expected, and we observe an overall weaker integrated brightness in the Herschel model compared to the ALMA model. The derived FWHM of the two models are consistent with each other, with the two models both having a weaker integrated brightness than the observation. Overall, the best-fitting model for the ALMA map is also consistent with the Herschel image at 70 μm.

Combining the updated orbit fit and disk analysis, we can study the alignment between the disk and the plane of the orbit of the companion. To do this, we calculate the misalignment angle with Equation (1) in Czekala et al. (2019) and the unconstrained relative astrometry fit from Section 3.2.1. The result is shown in Figure 12. The blue and yellow lines represent the front and back ambiguity between the disk and the orbit. This is because it is impossible to disambiguate between the orbital angular momentum vector pointing out of, or into, the plane of the sky. In either case, we find that the system is likely in a near-coplanar situation. Specifically, in the "front" case, where both angular momentum vectors point the same way relative to the plane of the sky, we report a 1σ confidence interval of $7°.0^{+17.1}_{-3.7}$. In the other case, we report a 1σ confidence interval of $15°.2^{+17.7}_{-4.8}$. The low-probability tail of significant misalignment in both cases can be traced back to the uncertainty in the companion's orbit. We further note that the more misaligned solutions also have higher eccentricity, which we consider to be less likely. Continuous astrometric monitoring will make this upper limit much more stringent if the disk and orbit are indeed close to coplanar.

We continue to explore the density structure of the disk from our findings. The density profiles of 100 fitting models selected from the converged part of the MCMC chain are plotted in the left panel of Figure 13. Interestingly, a number of models that satisfactorily fit the ALMA map have density profiles that extend down (even interior) to the current separation of the brown dwarf companion. This is physically implausible, as we expect the massive companion to clear out dust out to at least its apoastron distance. However, the fit to the ALMA map was not informed by the location and orbit of the companion, so it is reassuring to note that at least some of the models have peak
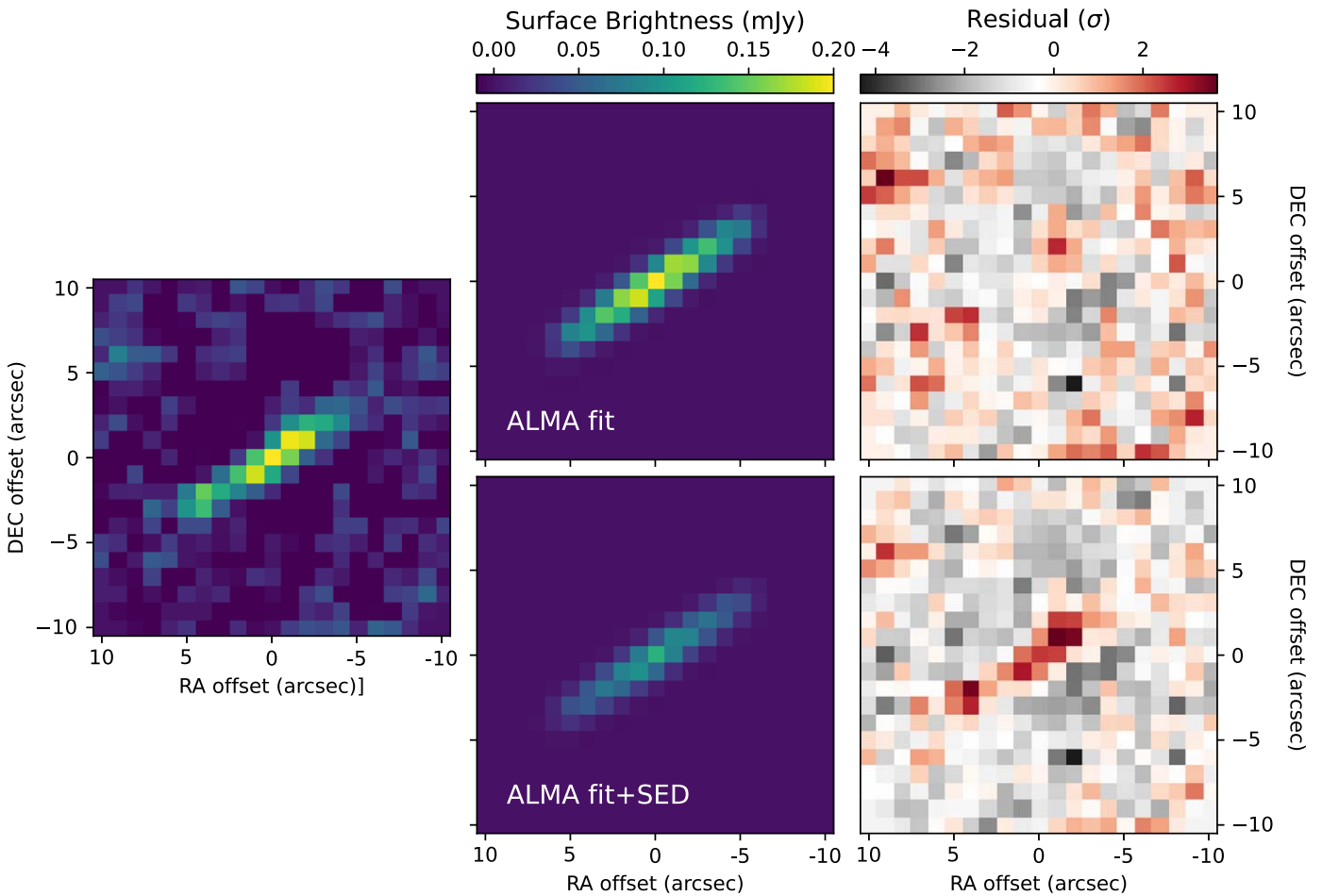
Figure 9. From left to right: ALMA map of the system binned to 1″ pixel; best-fit model to the ALMA data (top) and the model from the converged portion of the chain that best matches the SED (bottom, see Section 5.2); and residuals for both models. The ALMA maps uses the same color bar as the models. The ALMA fit agrees well with the model image, while the SED-selected model has an acceptable geometry but is significantly dimmer.

surface density radii that are exterior to the companion's orbit. Indeed, many of these models have significant amounts of dust close to the apoastron distance, suggesting that the brown dwarf may be directly interacting with it. Our SED selection in the following subsection provides additional support to this conclusion.

5.2. Best-fitting SED

So far, we have only considered the ALMA disk image in our analysis, but a holistic approach needs to consider multiple types of observation. An important piece of information is the spectral energy distribution (SED) of the disk. In their Herschel-based study, Moór et al. (2015) fit the SED and the image of the disk separately. The SED fit in Moór et al. (2015) yields a radius of 64 ± 6 au, which is about twice as large as the image fit (and also consistent with our fit results). A likely explanation for this discrepancy is the assumption in the SED fit that the dust is at blackbody equilibrium temperature. In debris disks, the smallest grains tend to superheat to a temperature that is significantly hotter. As a result, SED-informed disk radii are significantly smaller than those obtained from resolved imaging. This discrepancy has also been studied quantitatively with previous Herschel observations of entire samples of debris disks, and a clear trend with stellar luminosity has been shown (e.g., Morales et al. 2016). Given

the luminosity of HR 2562, we conclude that a factor-of-two discrepancy between SED- and image-fit disk radii is consistent with previous literature.

Nonetheless, our radiative transfer model, which self-consistently treats the cooling inefficiency of small dust grains, also predicts a system's SED so that we can in principle incorporate this observable in our analysis. This allows us to consider the SED of the models in the MCMC chain in order to assess whether more stringent constraints on the disk properties can be inferred. Unfortunately, we did not compute the SED during the chain, and this analysis must be conducted a posteriori. To examine this, we computed the SEDs of a selection of models that were included in the MCMC chain. Specifically, we randomly selected 1000 models from all the walkers in the lower-temperature chain between steps 1900 and 2000, where the chain was well converged. We then computed the χ^2 between the models and the observed SED (including the IRAS, Herschel, and ALMA fluxes) and selected the 100 best-fit models. To put the result of this SED selection in context, we also randomly selected 100 models from the same part of the chains and plotted their SEDs. The results are shown in Figure 14. Many of the models selected based exclusively on the ALMA image fit are poor fits to the SED, generally underestimating the 70–160 μm emission. Nonetheless, some models are good fits to the SED even though our model fitting was only informed by the ALMA image.
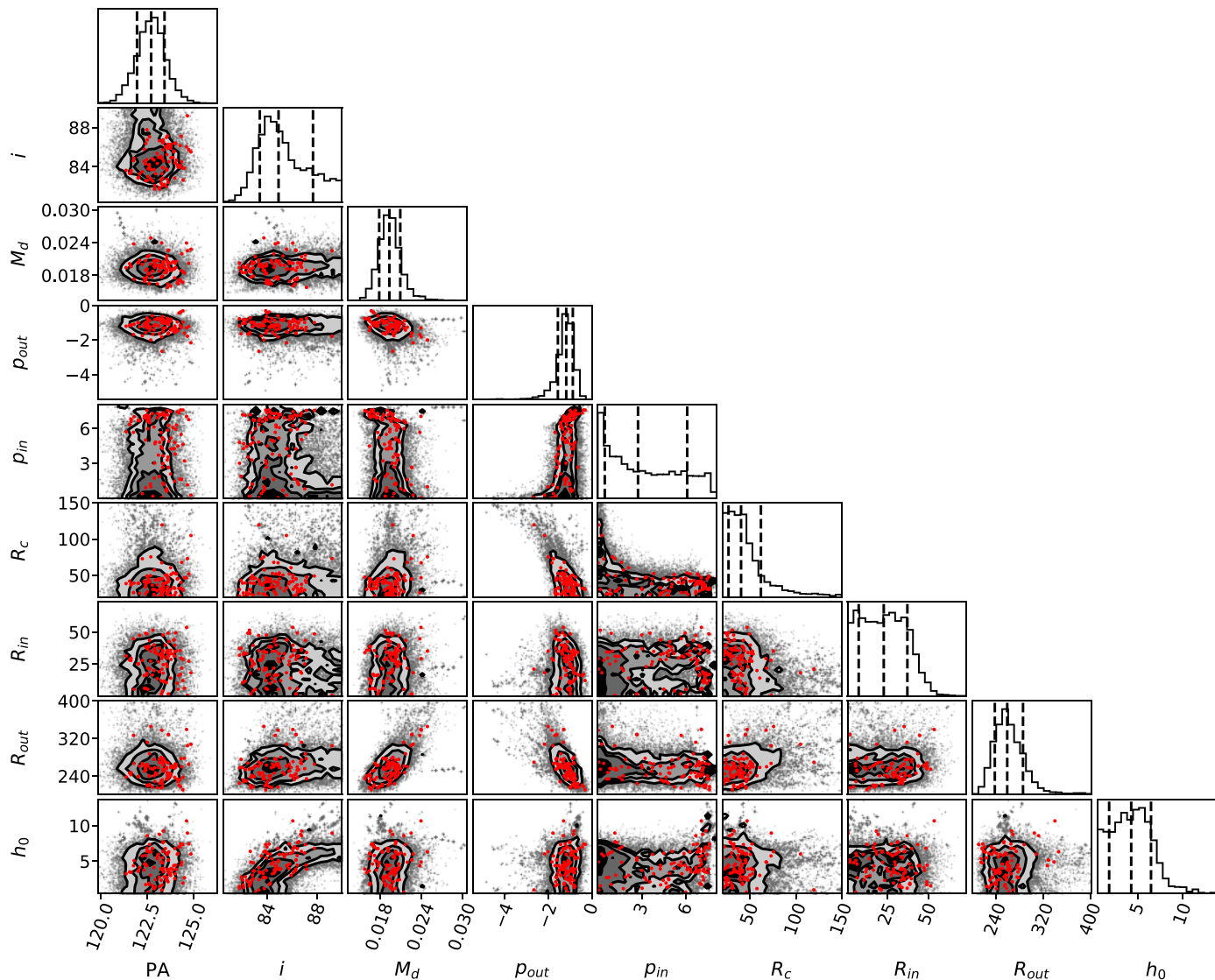
Figure 10. Results of the MCMC fit of the ALMA image of the HR 2562 disk properties. The corner plot, shown as gray dots and black density contours, is created from the last 1400 iterations of the chain, i.e., after convergence was reached. Contours represent the 1σ, 2σ, and 3σ confidence levels. The 100 models selected from the converging part of the chain that best fit the observed SED of the disk (see Section 5.2) are represented in red dots.
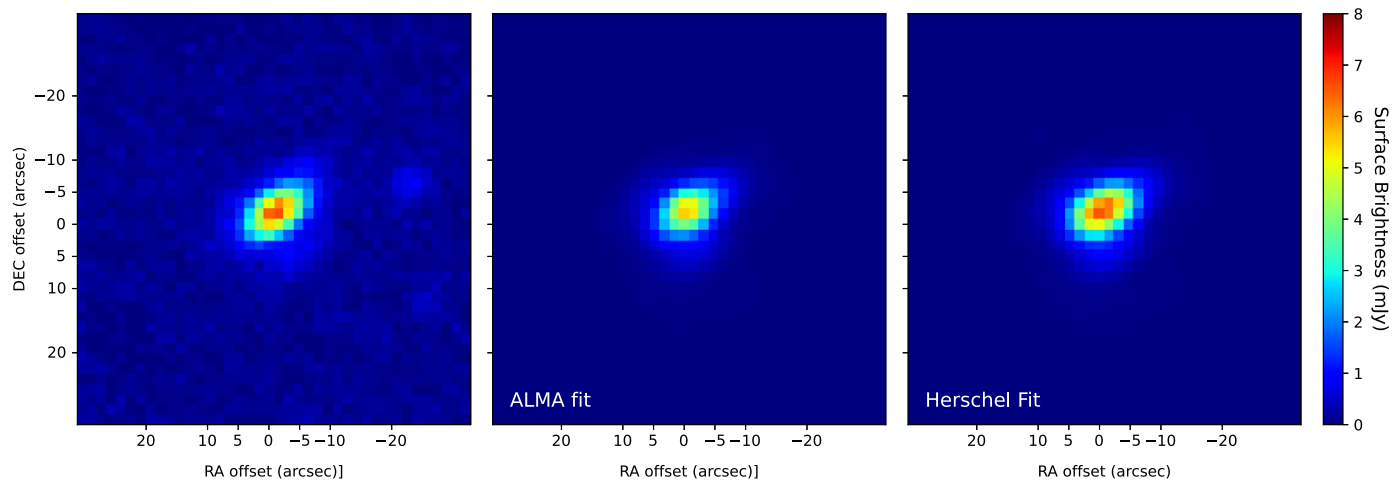

Figure 11. Observed (left panel; Moór et al. 2015) and synthetic (center and right panels) 70 μm Herschel image of HR 2562. The two models represent the model using the ALMA best-fit parameters from this study and the Herschel best-fit model from Moor et al.
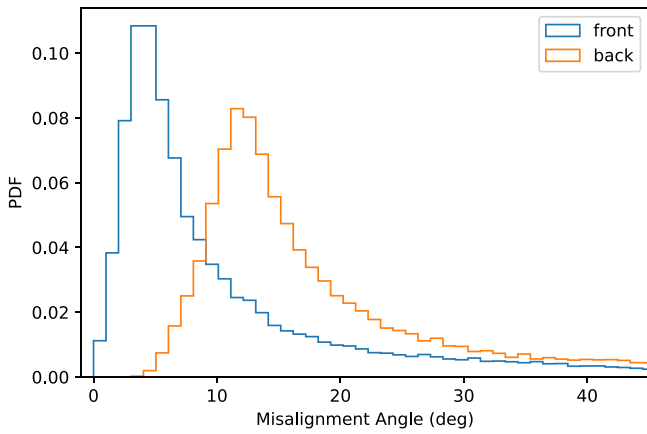
Figure 12. Relative inclination of the disk (as seen by ALMA) and the companion's orbit. The two histograms represent the two cases regarding the front/back ambiguity in both disk and orbital planes.

To gauge how well the best-fit SED model describes the ALMA image, we compare it with the best-fit image model and the data in Figure 10. The best-fit SED model does not fit the data as well, with a reduced χ^2 of 1.68 and the clump-like structure around the location of the star in the disk, indicating that the SED-fitting model produces a less centrally peaked surface brightness profile. To see the effect of SED rejection on the disk structures, we overplot the models selected by lower SED χ^2 with red dots in Figure 10. The main difference between the SED-selected models and the overall MCMC posteriors is that the former show a preference for larger values of $R_{\rm in}$. To illustrate this, we again compare the density profiles of 100 randomly selected models with those of the 100 best-fit SED models as seen in the right panel of Figure 13. The best-fit SED models almost universally have a peak surface density radius that is exterior to the apoastron distance of the companion. In other words, the best SED models prefer the family of models with an inner hole potentially consistent with truncation by the brown dwarf. This shows that the SED indeed provides useful information for us to narrow down the result from the ALMA image MCMC.

Overall, although our SED-selected models do not fit the ALMA image as well, they are consistent with strong dynamical interaction between the substellar companion and the debris disk, providing a new test bed for such interactions. Future work will require a simultaneous fit to the SED and resolved images of the disk in order to provide tighter and more consistent constraints of the exact architecture of the system.

5.3. Dynamical Interaction

A number of theoretical and numerical studies have tackled the problem of disk truncation by an interior substellar object, but none was tailored to the exact configuration of the HR 2562 system. The companion mass, for which we only have a dynamical upper limit and a model-dependent estimate, the companion semimajor axis, and the orbital eccentricity, which is only modestly constrained at this point, are three main factors that set the location of the disk's inner radius. Here, we will explore the predictions of several such models when applied to the parameter values estimated in this study. Relative inclination likely also plays a role, although most studies assume (near) coplanarity. Since this assumption is consistent

with all the data at hand for HR 2562, we can thus use these theoretical predictions to compare them to the geometry of the HR 2562 system and assess the likelihood that the brown dwarf companion is actively truncating the debris disk. It is worth pointing out that disk truncation studies sometimes rely on different criteria to define the inner edge, such as the "chaotic zone" (Quillen & Faber 2006; Chiang et al. 2009) or the "Hill sphere argument" (Pearce & Wyatt 2014), such that for a given set of parameters, there is a range of predicted inner radii for the truncated disk. Nonetheless, we can compare the range of predicted inner disk radii to the range derived from fitting our ALMA observations. Although there is a possibility that the companion's orbit may be highly eccentric, which could produce the clump we see in Figure 3 as well as an asymmetric disk, we do not think this is the likely scenario, due to the clump still being marginally consistent with a symmetric disk in brightness profile as well as the fact that the disk and the orbit are shown to align with each other (Figure 12). Thus, we only consider the case for low- to moderate-eccentricity orbits in the following analysis.

Given our limited constraint on the companion's orbit, we select three different values of eccentricity and derive the corresponding disk inner edge location. We obtain the corresponding semimajor axis from the orbit posterior distribution in Figure 7 and conservatively assume the upper limit of 18.5 $M_{\rm Jup}$ as the companion mass in our predictions. We first use an eccentricity of $e \sim 0.1$ (and a semimajor axis of 28 au) and adopt equation 16 from the Fomalhaut-tailored simulations of Chiang et al. (2009) that is designed for low-eccentricity systems. This yields an estimate of the disk's inner radius of 44 au. We also considered the analysis of Pearce & Wyatt (2014) and applied their Equations 9 and 10, assuming a semimajor axis of 28 au and an eccentricity of $e \sim 0.1$, to predict an inner radius of 54 au. Finally, we consider the result from the N-body disk simulations in Rodigas et al. (2014) for a more general framework using the same methodology, exploring explicitly a broader range of perturber masses and orbital eccentricities (up to $e = 0.2$). From their study, we adopt the $10\,M_J$ case, as it is the closest to the likely mass of HR 2562 B. Taking results from their Table 2 and adopting semimajor axes of 30 au and 24 au for the circular and $e = 0.2$ cases, we obtain respective predicted locations of the disk inner radius of 50.8 and 51.1 au. To compare the estimates with our models, we define the effective inner radius of our models as the half-peak point of their surface density. We compute the effective inner radii for 1000 models from the converged portion of the ALMA MCMC chain as well as the 100 best-fitting models by SED, and show the results alongside the above estimates in Figure 15.

All in all, existing dynamical models predict that the HR 2562 B mass and orbit should result in the exterior debris disk being truncated at about 45–55 au. Our ALMA observations suggest that disk extends at least that close to the brown dwarf, possibly even closer (see Figure 15). It is therefore extremely likely that the brown dwarf is directly responsible for the disk truncation, without the need for additional perturbers, as has been suggested for HD 206893. Given the limited orbital coverage and modest resolution of our ALMA observations, it is currently impossible to discriminate between the different models discussed above, but it is likely that further observations in the next few years will be able to produce observational constraints that allow for such a study. HR 2562 is therefore
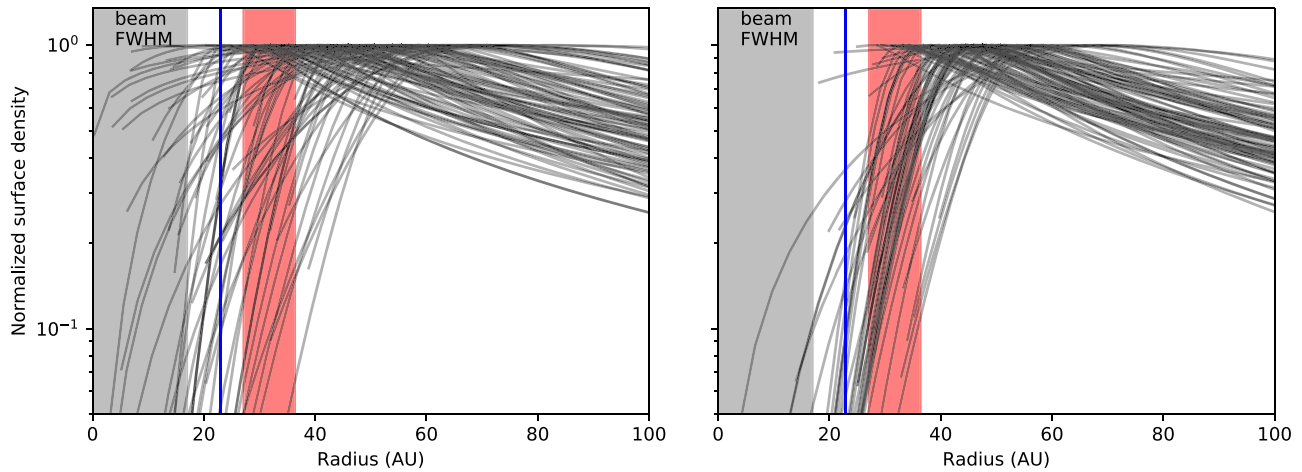
Figure 13. Left: density profiles of 100 randomly selected models from the converged part of the MCMC chain. Right: density profiles of SED-selected models (see Section 5.2). The density profiles in both panels are normalized to their maximum values, for ease of comparison. The blue line marks the separation of the brown dwarf at the time of the ALMA observations, while the red bar represent the 1σ range of apoastron distance of its orbit. The restriction of SED alone is enough to eliminate most models with R_{in} smaller than the current separation of the brown dwarf, which are physically implausible.
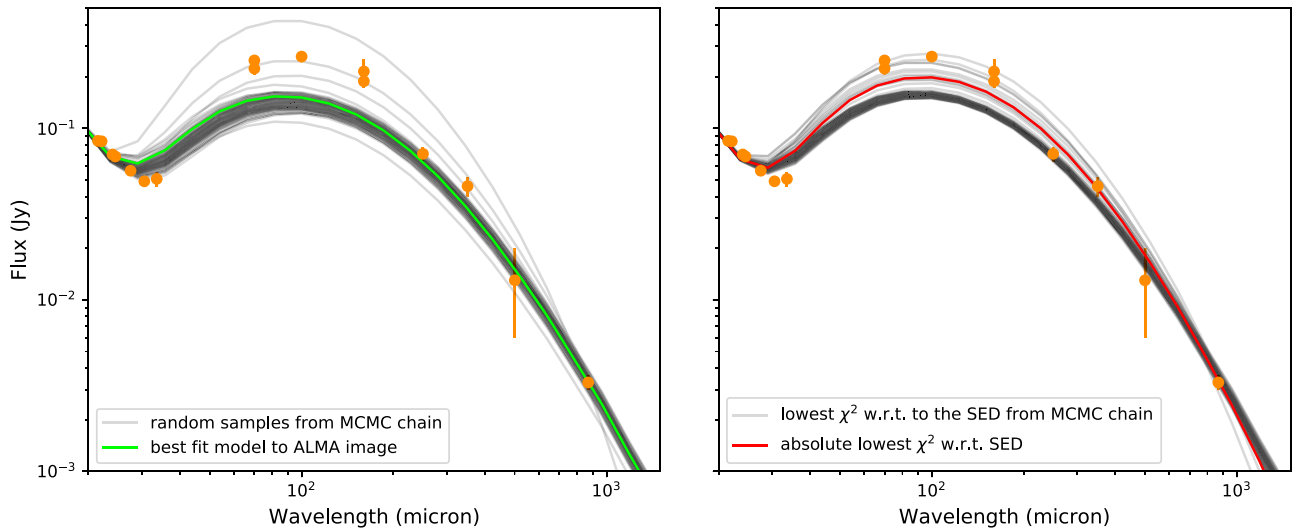
Figure 14. SED of HR 2562 (orange circles) compared to subsets of the models from the converged part of the ALMA map fitting MCMC chain. The left panel shows 100 models randomly selected from the chain without considering the SED, while the right panel shows the 100 models from the same portion of the chain with the least χ^2 with respect to the SED. The green solid line in the left panel represents the model with the best-fit model to the ALMA image, and the red solid line in the right panel represents the lowest χ^2 with respect to the measured SED.

bound to become a new test bed for dynamical studies of debris disk truncation by an interior substellar companion.

6. Conclusion

HR 2562 is an exciting system with a brown dwarf companion located inside the inner hole of a cold debris disk, making it a very likely candidate for dynamical sculpting between the disk and the companion. In this paper, we report the first ALMA 870 μm observations of the disk around HR 2562, as well as the continued GPI monitoring on the substellar companion's orbital motion, which is close to edge-on. Coupled with Gaia EDR3 observations of the star, we obtain improved constraints on the substellar companion orbital elements. In particular, the combined analysis of the absolute and relative astrometry of the system places a 3σ upper limit of 18.5 M_{jup} on the companion.

The new ALMA observations with an angular resolution roughly six times higher than previous Herschel observations

of the system achieved a peak signal-to-noise ratio of $\sim$7, enabling a more detailed study of the disk structure. Using radiative transfer modeling, we perform an MCMC fit of the disk key parameters and confirm the disk is seen at high inclination (3σ lower limit of $i > 79°\!.3$), consistent with previous studies of the system. We further compute the misalignment angle between the disk and the orbit and find that it is either $7^{+17°}_{-4}$ or $15^{+18°}_{-5}$, depending on unresolved ambiguities due to projection effects. This provides further evidence that the disk and the orbit are close to a coplanar configuration.

To test dynamical models of disk truncation by a low-mass companion, we focus on the location of the inner edge of the debris disk. Modeling of the ALMA map yields a 3σ upper limit of 62.3 au, as the resolution is insufficient to fully resolve the inner parts of the disk. We note, however, that consideration of the SED in the analysis further narrows the allowable range of inner disk radii and locates the latter at $\approx$30 au, albeit
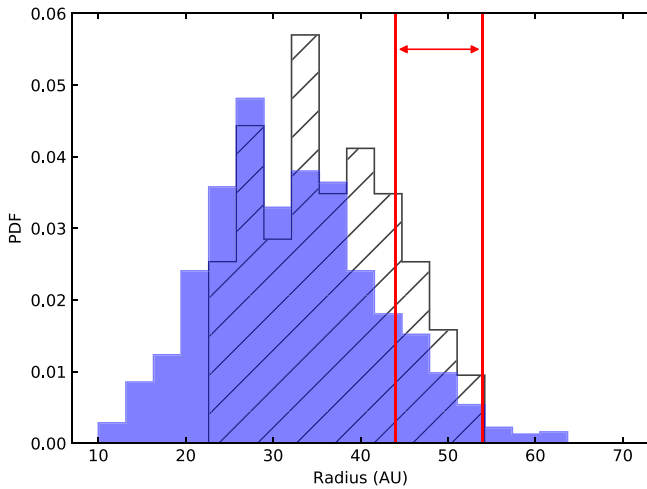
Figure 15. Distribution of inner disk radius for the 1000 randomly selected models from the converged part of the ALMA MCMC fit and the 100 best-fitting models by SED are plotted (solid and hatched histograms, respectively). The red arrows and lines mark the range of predicted disk inner edge locations using the dynamical models from Chiang et al. (2009), Pearce & Wyatt (2014), and Rodigas et al. (2014).

with a significant uncertainty. This is close to the apoastron distance derived from our orbital fit, providing further evidence for the companion dynamically sculpting the disk. We further test three disk truncation models, which predict the location of the disk inner radius to be in the 45–55 au range based on the companion's orbit and estimated mass. The image-derived inner radius is even closer to the companion, possibly pointing to a lower mass estimate for the companion and/or to shortcoming in the models.

HR 2562 presents a unique opportunity to quantitatively test disk truncation models, provided the system's architecture can be further constrained. Continued monitoring of the companion's orbit with high-contrast imaging instruments and of the reflex motion of the host star with Gaia will yield increasingly precise estimates of the orbit geometry as well as the first dynamical measurement of the companion's mass. Deeper and higher-resolution images with ALMA, as well as a simultaneous fit to the submillimeter map and the system's SED, will provide a better-defined view of the disk's inner regions, directly testing dynamical models.

Appendix A
GAIA Goodness-of-fit Metric

The GAIA EDR3 catalog provides a number of statistical tools that can be used to analyze the quality of the astrometric fit. Since the GAIA precision is sensitive to the brightness of the star, in Figure 16, we present key diagnostic metrics to evaluate the quality of the HR 2562 EDR3 entry. Overall, the star appears well behaved, albeit with a small but significant astrometric excess noise of 0.158 mas. It is not clear if this excess noise is astrophysical in nature, but the excess noise is significantly lower than reported in the Hipparcos catalog (2.4 mas). Overall, we consider the GAIA data to be of good quality, i.e., the data show no strong evidence for departure from a linear motion over the course of the GAIA observations.
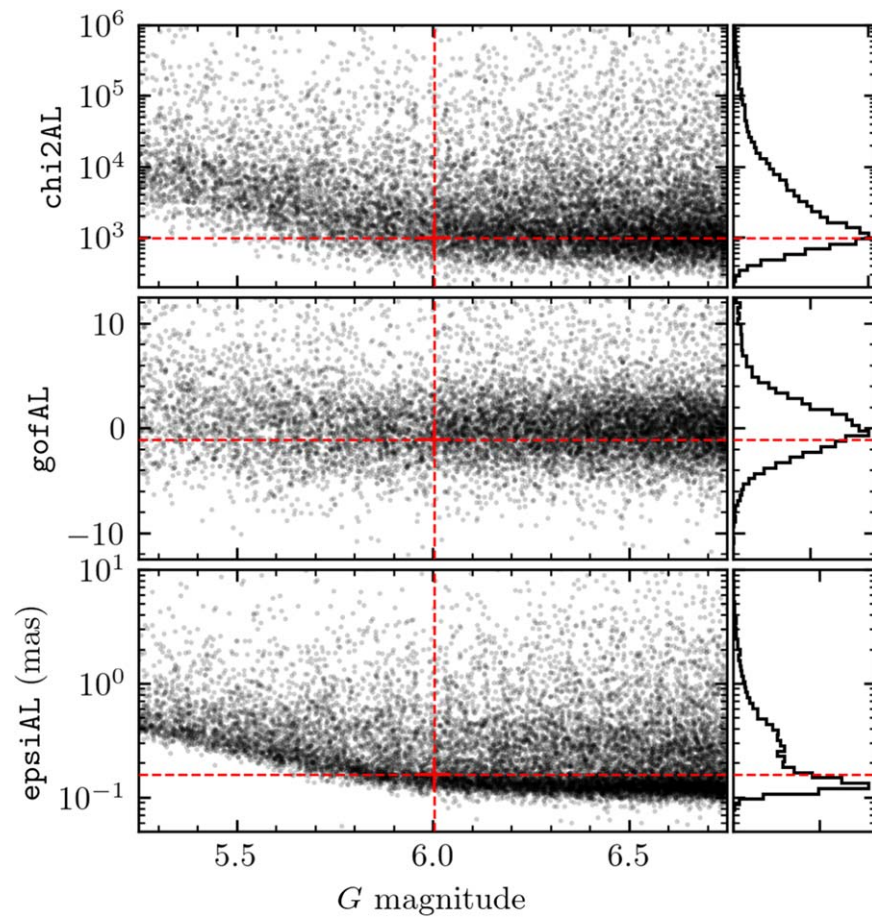
Figure 16. Goodness-of-fit metrics for HR 2562 (red cross) compared with other Gaia sources of a similar G magnitude (dark points). The top two panels give the χ^2 and a goodness-of-fit metric, while the bottom panel gives the amplitude of the residuals to a five-parameter fit that assumes linear space motion. The distributions of these three parameters are shown on the right. Large values for any of these parameters can be used as an indication of nonlinear motion between mid-2015 and mid-2017 caused by an orbiting companion.

Appendix B
Full Orbital Fit

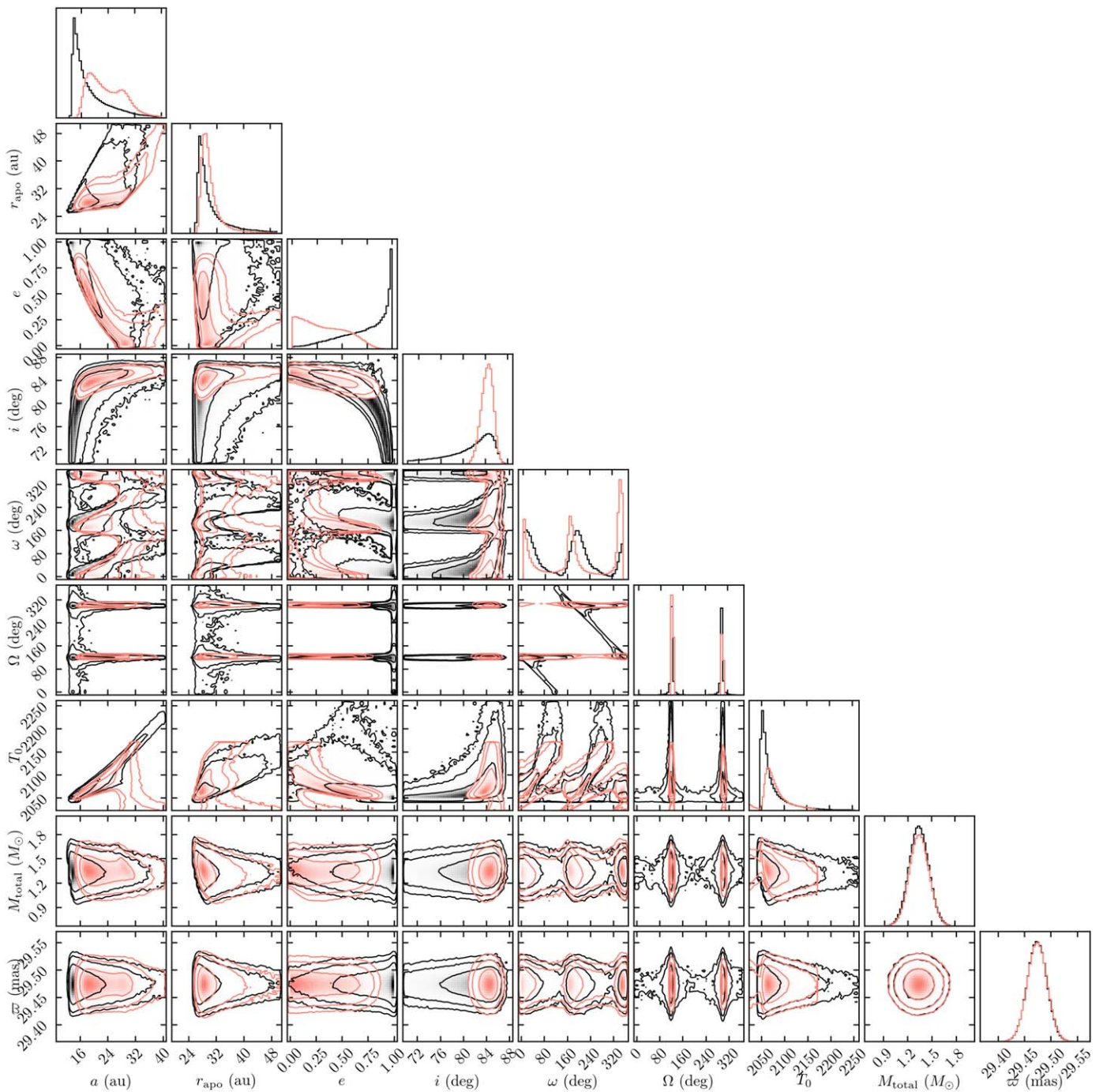In Figure 17, we present the full corner plot of the HR 2562 B orbit MCMC run in Section 3.2.2.

Figure 17. Full corner plot of HR2562 orbit with and without the new constraints from the ALMA fit. Contours represent the 1σ, 2σ, and 3σ confidence levels.

ORCID iDs

Stella Yimiao Zhang ⓘ https://orcid.org/0000-0003-2122-6714

Gaspard Duchêne ⓘ https://orcid.org/0000-0002-5092-6464

Robert J. De Rosa ⓘ https://orcid.org/0000-0002-4918-0247

Megan Ansdell ⓘ https://orcid.org/0000-0003-4142-9842

Quinn Konopacky ⓘ https://orcid.org/0000-0002-9936-6285

Thomas Esposito ⓘ https://orcid.org/0000-0002-0792-3719

Eugene Chiang ⓘ https://orcid.org/0000-0002-6246-2310

Malena Rice ⓘ https://orcid.org/0000-0002-7670-670X

Brenda Matthews ⓘ https://orcid.org/0000-0003-3017-9577

Paul Kalas ⓘ https://orcid.org/0000-0002-6221-5360

Bruce Macintosh ⓘ https://orcid.org/0000-0003-1212-7538

Franck Marchis ⓘ https://orcid.org/0000-0001-7016-7277

Stan Metchev ⓘ https://orcid.org/0000-0003-3050-8203

Julien Rameau ⓘ https://orcid.org/0000-0003-0029-0258

Kimberly Ward-Duong ⓘ https://orcid.org/0000-0002-4479-8291

Schuyler Wolff ⓘ https://orcid.org/0000-0002-9977-8255

Michael P. Fitzgerald ⓘ https://orcid.org/0000-0002-0176-8973

Vanessa P. Bailey ⓘ https://orcid.org/0000-0002-5407-2806

Travis S. Barman ⓘ https://orcid.org/0000-0002-7129-3002

Christine H. Chen ⓘ https://orcid.org/0000-0002-8382-0447

Jeffrey K. Chilcotte ⓘ https://orcid.org/0000-0001-6305-7272

Tara Cotten ⓘ https://orcid.org/0000-0003-0156-3019

René Doyon ⓘ https://orcid.org/0000-0001-5485-4675

Katherine B. Follette ⓘ https://orcid.org/0000-0002-7821-0695

Benjamin L. Gerard ⓘ https://orcid.org/0000-0003-3978-9195

Stephen Goodsell ⓘ https://orcid.org/0000-0002-4144-5116

Alexandra Z. Greenbaum ⓘ https://orcid.org/0000-0002-7162-8036

Pascale Hibon ⓘ https://orcid.org/0000-0003-3726-5494

Patrick Ingraham ⓘ https://orcid.org/0000-0003-3715-8138

Mark S. Marley ⓘ https://orcid.org/0000-0002-5251-2943

Christian Marois ⓘ https://orcid.org/0000-0002-4164-4182

Maxwell A. Millar-Blanchaer ⓘ https://orcid.org/0000-0001-6205-9233

Eric L. Nielsen ⓘ https://orcid.org/0000-0001-6975-9056

Rebecca Oppenheimer ⓘ https://orcid.org/0000-0001-7130-7681

Marshall D. Perrin ⓘ https://orcid.org/0000-0002-3191-8151

Abhijith Rajan ⓘ https://orcid.org/0000-0002-9246-5467

Fredrik T. Rantakyrö ⓘ https://orcid.org/0000-0002-9667-2244

Jean-Baptiste Ruffio ⓘ https://orcid.org/0000-0003-2233-4821

Dmitry Savransky ⓘ https://orcid.org/0000-0002-8711-7206

Adam C. Schneider ⓘ https://orcid.org/0000-0002-6294-5937

Anand Sivaramakrishnan ⓘ https://orcid.org/0000-0003-1251-4124

Inseok Song ⓘ https://orcid.org/0000-0002-5815-7372

Remi Soummer ⓘ https://orcid.org/0000-0003-2753-2819

Sandrine Thomas ⓘ https://orcid.org/0000-0002-9121-3436

Jason J. Wang ⓘ https://orcid.org/0000-0003-0774-6502

Sloane J. Wiktorowicz ⓘ https://orcid.org/0000-0003-4483-5037

References

Augereau, J. C., Lagrange, A. M., Mouillet, D., Papaloizou, J. C. B., & Grorod, P. A. 1999, A&A, 348, 557

Augereau, J. C., Nelson, R. P., Lagrange, A. M., Papaloizou, J. C. B., & Mouillet, D. 2001, A&A, 370, 447

Casagrande, L., Schönrich, R., Asplund, M., et al. 2011, A&A, 530, A138

Chauvin, G., Gratton, R., Bonnefoy, M., et al. 2018, A&A, 617, A76

Chiang, E., Kite, E., Kalas, P., Graham, J. R., & Clampin, M. 2009, ApJ, 693, 734

Chilcote, J. K., Larkin, J. E., Maire, J., et al. 2012, Proc. SPIE, 8446, 84468W

Czekala, I., Chiang, E., Andrews, S. M., et al. 2019, ApJ, 883, 22

Dawson, R. I., Murray-Clay, R. A., & Fabrycky, D. C. 2011, ApJL, 743, L17

De Rosa, R. J., Dawson, R., & Nielsen, E. L. 2020a, A&A, 640, A73

De Rosa, R. J., Nguyen, M. M., Chilcote, J., et al. 2020c, JATIS, 6, 015006

De Rosa, R. J., Nielsen, E. L., Wang, J. J., et al. 2020b, AJ, 159, 1

Dohnanyi, J. S. 1969, JGR, 74, 2531

Draine, B. T., & Lee, H. M. 1984, ApJ, 285, 89

Esposito, T. M., Duchêne, G., Kalas, P., et al. 2018, AJ, 156, 47

Esposito, T. M., Kalas, P., Fitzgerald, M. P., et al. 2020, AJ, 160, 24

Ferrer-Chávez, R., Wang, J. J., & Blunt, S. 2021, AJ, 161, 241

Foreman-Mackey, D., Hogg, D. W., Lang, D., & Goodman, J. 2013, PASP, 125, 306

Gaia Collaboration, Brown, A. G. A., Vallenari, A., et al. 2021, A&A, 649, A1

Gray, R. O., Corbally, C. J., Garrison, R. F., et al. 2006, AJ, 132, 161

Konopacky, Q. M., Rameau, J., Duchêne, G., et al. 2016, ApJL, 829, L4

Lagrange, A. M., Bonnefoy, M., Chauvin, G., et al. 2010, Sci, 329, 57

Lagrange, A. M., Kasper, M., Boccaletti, A., et al. 2009, A&A, 506, 927

Larkin, J. E., Chilcote, J. K., Aliado, T., et al. 2014, Proc. SPIE, 9147, 91471K

Lindegren, L., Klioner, S. A., Hernández, J., et al. 2021, A&A, 649, A2

Lucy, L. B. 2014, A&A, 563, A126

Macintosh, B., Graham, J. R., Ingraham, P., et al. 2014, PNAS, 111, 12661

Madurowicz, A., Macintosh, B. A., Ruffio, J.-B., et al. 2018, Proc. SPIE, 10703, 107036E

Maire, A. L., Rodet, L., Lazzoni, C., et al. 2018, A&A, 615, A177

Marino, S., Zurlo, A., Faramaz, V., et al. 2020, MNRAS, 498, 1319

Marois, C., Lafrenière, D., Doyon, R., Macintosh, B., & Nadeau, D. 2006, ApJ, 641, 556

McMullin, J. P., Waters, B., Schiebel, D., Young, W., & Golap, K. 2007, in ASP Conf. Ser. 376, Astronomical Data Analysis Software and Systems XVI, ed. R. A. Shaw, F. Hill, & D. J. Bell (San Francisco, CA: ASP), 127

Mesa, D., Baudino, J. L., Charnay, B., et al. 2018, A&A, 612, A92

Moór, A., Kóspál, Á., Ábrahám, P., et al. 2015, MNRAS, 447, 577

Moór, A., Ábrahám, P., Derekas, A., et al. 2006, ApJ, 644, 525

Morales, F. Y., Bryden, G., Werner, M. W., & Stapelfeldt, K. R. 2016, ApJ, 831, 97

Musso Barcucci, A., Launhardt, R., Kennedy, G. M., et al. 2019, A&A, 627, A77

Nederlander, A., Hughes, A. M., Fehr, A. J., et al. 2021, ApJ, 917, 5

O'Neil, K. K., Martinez, G. D., Hees, A., et al. 2019, AJ, 158, 4

Pawellek, N., & Krivov, A. V. 2015, MNRAS, 454, 3207

Pearce, T. D., & Wyatt, M. C. 2014, MNRAS, 443, 2541

Pearce, T. D., Wyatt, M. C., & Kennedy, G. M. 2015, MNRAS, 448, 3679

Pecaut, M. J., & Mamajek, E. E. 2013, ApJS, 208, 9

Perrin, M. D., Maire, J., Ingraham, P., et al. 2014, Proc. SPIE, 9147, 91473J

Pinte, C., Ménard, F., Duchêne, G., & Bastien, P. 2006, A&A, 459, 797

Poyneer, L. A., De Rosa, R. J., Macintosh, B., et al. 2014, Proc. SPIE, 9148, 91480K

Poyneer, L. A., Palmer, D. W., Macintosh, B., et al. 2016, ApOpt, 55, 323

Pueyo, L., Soummer, R., Hoffmann, J., et al. 2015, ApJ, 803, 31

Quillen, A. C., & Faber, P. 2006, MNRAS, 373, 1245

Racine, R., Walker, G. H., Nadeau, D., Doyon, R., & Marois, C. 1999, PASP, 111, 587

Rodigas, T. J., Malhotra, R., & Hinz, P. M. 2014, ApJ, 780, 65

Sivaramakrishnan, A., & Oppenheimer, B. R. 2006, ApJ, 647, 620

Smith, W. H. 1987, PASP, 99, 1344

Soummer, R., Pueyo, L., & Larkin, J. 2012, ApJL, 755, L28

Soummer, R., Sivaramakrishnan, A., Pueyo, L., Macintosh, B., & Oppenheimer, B. R. 2011, ApJ, 729, 144

Su, K. Y. L., De Buizer, J. M., Rieke, G. H., et al. 2017, AJ, 153, 226

Tsiganis, K. 2010, EPJST, 186, 67

van Leeuwen, F. 2007a, A&A, 474, 653

van Leeuwen, F. 2007b, in Hipparcos, the New Reduction of the Raw Data, ed. F. Leeuwen, Vol. 350 (Dordrecht: Springer),

Wang, J. J., Graham, J. R., Pueyo, L., et al. 2016, AJ, 152, 97

Wang, J. J., Perrin, M. D., Savransky, D., et al. 2018, JATIS, 4, 018002

Wang, J. J., Ruffio, J.-B., De Rosa, R. J., et al. 2015, pyKLIP: PSF Subtraction for Exoplanets and Disks, Astrophysics Source Code Library, ascl:1506.001

Wang, J. J., Ruffio, J.-B., Morris, E., et al. 2021, AJ, 162, 148

Wilner, D. J., MacGregor, M. A., Andrews, S. M., et al. 2018, ApJ, 855, 56